

Northumbria Research Link

Citation: Vreugdenhil, Catherine A., Taylor, John R., Davis, Peter E. D., Nicholls, Keith W., Holland, Paul R. and Jenkins, Adrian (2022) The ocean boundary layer beneath Larsen C Ice Shelf: insights from large-eddy simulations with a near-wall model. *Journal of Physical Oceanography*, 52 (8). pp. 1903-1926. ISSN 0022-3670

Published by: American Meteorological Society

URL: <https://doi.org/10.1175/jpo-d-21-0166.1> <<https://doi.org/10.1175/jpo-d-21-0166.1>>

This version was downloaded from Northumbria Research Link:
<https://nrl.northumbria.ac.uk/id/eprint/49192/>

Northumbria University has developed Northumbria Research Link (NRL) to enable users to access the University's research output. Copyright © and moral rights for items on NRL are retained by the individual author(s) and/or other copyright owners. Single copies of full items can be reproduced, displayed or performed, and given to third parties in any format or medium for personal research or study, educational, or not-for-profit purposes without prior permission or charge, provided the authors, title and full bibliographic details are given, as well as a hyperlink and/or URL to the original metadata page. The content must not be changed in any way. Full items must not be sold commercially in any format or medium without formal permission of the copyright holder. The full policy is available online: <http://nrl.northumbria.ac.uk/policies.html>

This document may differ from the final, published version of the research and has been made available online in accordance with publisher policies. To read and/or cite from the published version of the research, please visit the publisher's website (a subscription may be required.)



**Northumbria
University**
NEWCASTLE



UniversityLibrary

1 **The ocean boundary layer beneath Larsen C Ice Shelf: insights from**
2 **large-eddy simulations with a near-wall model**

3 Catherine A. Vreugdenhil*

4 *University of Cambridge, Cambridge, UK and the University of Melbourne, Melbourne, Australia*

5 John R. Taylor

6 *University of Cambridge, Cambridge, UK*

7 Peter E. D. Davis, Keith W. Nicholls, Paul R. Holland

8 *British Antarctic Survey, Cambridge, UK*

9 Adrian Jenkins

10 *Northumbria University, Newcastle upon Tyne, UK*

11 *Corresponding author address: Department of Mechanical Engineering, University of Melbourne,

12 Melbourne, Australia

13 E-mail: cat.vreugdenhil@unimelb.edu.au

ABSTRACT

14 The melt rate of Antarctic ice shelves is of key importance for rising sea
15 levels and future climate scenarios. Recent observations beneath Larsen C Ice
16 Shelf revealed an ocean boundary layer that was highly turbulent and raised
17 questions on the effect of these rich flow dynamics on the ocean heat trans-
18 fer and the ice shelf melt rate (Davis and Nicholls 2019). Directly motivated
19 by the field observations, we have conducted large-eddy simulations (LES) to
20 further examine the ocean boundary layer beneath Larsen C Ice Shelf. The
21 LES was initialised with uniform temperature and salinity (T/S) and included
22 a realistic tidal cycle and a small basal slope. A new parameterization based
23 on Vreugdenhil and Taylor (2019) was applied at the top boundary to model
24 near-wall turbulence and basal melting. The resulting vertical T/S profiles,
25 melt rate and friction velocity matched well with the Larsen C Ice Shelf ob-
26 servations. The instantaneous melt rate varied strongly with the tidal cycle,
27 with faster flow increasing the turbulence and mixing of heat towards the ice
28 base. An Ekman layer formed beneath the ice base and, due to the strong
29 vertical shear of the current, Ekman rolls appeared in the mixed layer and
30 stratified region (depth $\approx 20 - 60\text{m}$). In an additional high-resolution simula-
31 tion (conducted with a smaller domain) the Ekman rolls were associated with
32 increased turbulent kinetic energy, but a relatively small vertical heat flux.
33 Our results will help with interpreting field observations and parameterizing
34 the ocean-driven basal melting of ice shelves.

35 **1. Introduction**

36 The melt rate of Antarctic ice shelves is expected to play a crucial role in determining global
37 sea level rise in the future. Ice shelves are the floating extensions of ice sheets and act to buttress
38 grounded ice (Schoof 2007). Thinning of ice shelves can destabilise the marine-based regions
39 of the ice sheet, causing grounded ice flow to accelerate and thereby raising the sea level. In
40 a changing climate, altered winds can enhance the flow of warm waters towards ice shelves, for
41 example in the Weddell Sea (Hellmer et al. 2012; Darelius et al. 2016) and Amundsen Sea (Jenkins
42 et al. 2018; Holland et al. 2019). Warming the waters beneath Antarctic ice shelves will enhance
43 their basal melting (Shepherd et al. 2004; Pritchard et al. 2012; Paolo et al. 2015). However, the
44 turbulent ice shelf/ocean boundary layer mechanisms that physically transport heat towards the
45 ice base are not well constrained and remain a source of major uncertainty in predicting future sea
46 level (Dinniman et al. 2016). Here, we use large-eddy simulations (LES) of the ocean beneath an
47 ice shelf to examine the influence of turbulence and stratification on the melt rate.

48 Observations of the basal melting of Antarctic ice shelves have traditionally been sparse due
49 to the difficulty in observing these regions. Recently, borehole observations taken at Larsen C
50 Ice Shelf (Figure 1a) provided a glimpse of the rich dynamics in the underlying ocean (Nicholls
51 et al. 2012; Davis and Nicholls 2019). These measurements took place over more than a year and
52 were the first extended observations of small-scale turbulence beneath an ice shelf. Turbulence
53 instrument clusters placed at depths of 2.5m and 13.5m showed strong turbulence consistent with
54 a logarithmic “law-of-the-wall” boundary layer (e.g. Pope 2000). The observations also revealed
55 a spring-neap tidal signal superimposed on a weaker background flow, with the level of turbulence
56 closely tied to the tidal cycle. CTD (conductivity-temperature-depth) profiles showed a cold and
57 salty ocean with a well-mixed layer beneath the ice base (to ~ 50 m depth) followed by weak

58 stratification in both salinity and temperature (to ~ 80 m depth) and a uniform temperature and
59 salinity far-field ocean below. A year-averaged basal melt rate of 0.7 m/yr was measured using
60 upward-looking sonar. The Larsen C Ice Shelf borehole measurements provided evidence that
61 the water flowing into the sub-ice cavity (from the southeast) was cold High Salinity Shelf Water,
62 rather than the relatively warmer Modified Warm Deep Water observed outside the cavity in ship-
63 based measurements (Nicholls et al. 2012; Bathmann et al. 1994; Nicholls et al. 2004).

64 Since the borehole observations sampled a fixed position beneath the ice shelf, it was not clear
65 to what extent the local stratification reflects a local balance between melting and vertical mixing,
66 or whether upstream advection plays a significant role. This distinction is important when de-
67 veloping parameterizations for turbulence in the ice-shelf/ocean boundary layer and for planning
68 observational campaigns. Here, we use LES closely based on the observations from Davis and
69 Nicholls (2019) to study *locally* (by this we mean a purely vertical balance) generated turbulence
70 and stratification beneath Larsen C Ice Shelf. However, it is important to note that, even if the
71 stratification can be explained by a local balance, there is no guarantee that this solution is unique.
72 It is possible that the same T/S profiles could also be obtained through non-local processes.

73 Recent years have also seen other observational campaigns begin to characterise the ocean
74 boundary layer beneath different Antarctic ice shelves. For example, indirect measurements of
75 flow in the cold ocean cavity beneath Ronne Ice Shelf imply strong turbulence, weak stratification
76 and relatively low melt rates (Jenkins et al. 2010). These features are in common with observations
77 of Fimbul Ice Shelf (Hattermann et al. 2012) and regions of Ross Ice Shelf (Arzeno et al. 2014).
78 Other borehole observations with turbulence measurements have revealed more strongly stratified
79 regions and evidence of double-diffusion beneath George VI Ice Shelf (Kimura et al. 2015) and
80 near the grounding line of Ross Ice Shelf (Begeman et al. 2018). Pine Island Glacier Ice Shelf also
81 has regions of very strong stratification in the underlying ocean, as revealed by an autonomous

82 underwater vehicle (Stanton et al. 2013; Kimura et al. 2016). Our LES will have implications for
 83 sub-ice shelf circulations similar to that beneath Larsen C Ice Shelf and will help to explain some
 84 of the differences between sub-ice shelf circulations around Antarctica.

85 The physical processes involved in the melting of ice shelves, including turbulent mixing of heat
 86 and salt towards the ice, typically require parameterization in ocean models because they occur on
 87 length scales far smaller than the model resolution. The three-equation model is a common melt
 88 parameterization used in coarser ocean models or with observations further from the ice (McPhee
 89 et al. 1987; Jenkins 1991; Holland and Jenkins 1999; Malyarenko et al. 2020). This model is based
 90 on the conservation of heat (Eqn. 1) and salt (Eqn. 2), along with an equation for the freezing point
 91 of water (Eqn. 3),

$$c_w \rho_w C_d^{1/2} U \Gamma_T (T - T_b) = \rho_i L_i m, \quad (1)$$

$$\rho_w C_d^{1/2} U \Gamma_S (S - S_b) = \rho_i S_b m, \quad (2)$$

$$T_b = \lambda_1 S_b + \lambda_2 + \lambda_3 P. \quad (3)$$

94 Heat conduction into the ice has been neglected, which is a condition regularly used with the
 95 assumption that the conducted heat flux is small compared to the latent heat flux (Holland and
 96 Jenkins 1999). Inputs into the above formulation are the flow speed, U , temperature, T , and
 97 salinity, S , which are evaluated at a specific depth. Outputs are the temperature, T_b , and salinity,
 98 S_b , at the boundary and the melt rate, m . However, choices still need to be made in setting realistic
 99 drag coefficients, C_d , and heat, Γ_T , and salt, Γ_S , transfer coefficients. Other constants are the
 100 specific heat capacity of water, c_w , the latent heat of fusion, L_i , reference densities of ice, ρ_i , and
 101 water, ρ_w , pressure, P , and coefficients in a linearised expression for the freezing point of seawater,
 102 λ_1 , λ_2 and λ_3 (Jenkins 2011). Drag and transfer coefficients can be chosen to reproduce observed
 103 time-averaged melt rates, for example the three-equation model does a reasonable job of predicting

104 melt rates for Larsen C Ice Shelf (Davis and Nicholls 2019) and Ronne Ice Shelf (Jenkins et al.
105 2010). The three-equation model does less well when applied to sites with stronger stratification
106 and double-diffusion (Kimura et al. 2015; Begeman et al. 2018). It is crucial to have accurate melt
107 parameterizations to model future climate scenarios, but to achieve this we need to first understand
108 the processes determining the ice shelf melt rate.

109 There are many physical processes influencing the ocean beneath ice shelves, several of which
110 have been examined using idealised laboratory or numerical models. These include the meltwater
111 plume for a vertical (Gayen et al. 2016; McConnochie and Kerr 2016) or sloped (McConnochie
112 and Kerr 2018; Mondal et al. 2019) ice face, double-diffusion (Martin and Kauffman 1977; Keitzl
113 et al. 2016; Middleton et al. 2021; Rosevear et al. 2021) and stratification (Vreugdenhil and Taylor
114 2019). A one-dimensional model of the ocean beneath a melting ice shelf, which included the
115 Earth's rotation, stratification and a meltwater plume, revealed the impact of an Ekman layer and
116 strong across-slope flow (Jenkins 2016, 2021). By necessity, turbulent mixing was parameterized
117 in this one-dimensional model, but we might anticipate three-dimensional turbulent structures
118 to emerge in the ice-shelf/ocean boundary layer. For example, Deusebio et al. (2014) observed
119 Ekman rolls in numerical simulations of a weakly stratified Ekman layer. These structures are
120 the nonlinear manifestation of linear instabilities of an Ekman spiral, where the turning of the
121 horizontal velocity with depth creates an inflection point in the speed profile that can become
122 unstable (Lilly 1966; Fallor and Kaylor 1966; Brown 1972).

123 The defining feature of LES is explicitly resolving the most energetic three-dimensional turbu-
124 lence, while parameterizing only the smaller motions with a sub-grid scale model. Here, LES is
125 used to study the combined effects of the Earth's rotation, tides, and turbulence beneath a weakly-
126 sloped ice base under conditions consistent with Larsen C Ice Shelf observations reported in Davis
127 and Nicholls (2019). Our approach was to isolate a few key physical processes present in the obser-

128 vations (e.g. realistic tidal forcing, dynamic melting), while excluding processes whose presence
129 was inconclusive in the observations (e.g. large-scale horizontal temperature/salinity gradients,
130 double-diffusion). Comparing the LES results to the observations shows the relative importance
131 of the processes that are captured and those that are missing. By reducing the model physics we
132 also learn about the fluid dynamics that might be obscured by including additional physical pro-
133 cesses. A newly derived near-wall model parameterized turbulence near the ice base, as outlined
134 in Section 2. The LES are compared with Larsen C Ice Shelf observations in Section 3. The re-
135 sults provide new insight into the bulk properties of the boundary layer, the formation of Ekman
136 rolls and the transport of heat towards the ice base by boundary layer turbulence. In Section 4, the
137 results are discussed further in the context of the surrounding ocean dynamics, paving the way for
138 future observational and modelling studies. Conclusions are in Section 5.

139 **2. Model design**

140 The ocean beneath a melting ice shelf was modelled using idealised large-eddy simulations
141 (Figure 1). The initial and boundary conditions, along with other relevant simulation parameters
142 (details in Section 2a), closely followed field observations from December 2011 to January 2013
143 in the Southern region of Larsen C Ice Shelf. Nicholls et al. (2012) and Davis and Nicholls (2019)
144 (DN19) include full details of the observations. The model domain was tilted such that the top
145 boundary was aligned with the sloping ice base. There were periodic boundary conditions in the
146 two directions parallel to the ice base. A near-wall parameterization was applied as a boundary
147 condition at the top of the domain, which resulted in a spatially and temporally varying basal melt
148 rate (details in Section 2b). The lower boundary condition was impenetrable and free-slip, with
149 no-flux conditions for temperature and salinity.

150 Tidal forcing was applied through a pressure gradient to match the three strongest observed tidal
151 constituents (O1, K1 and M2) that resulted in a strong spring-neap cycle. The rectangular model
152 domain was sloped away from the horizontal by 0.5° to match the weak slope at the observational
153 site (based on Bedmap2, Fretwell et al. 2013). While the strong tides were hypothesised to set
154 the flow, the slope was matched to allow for the possibility of a meltwater plume. The Coriolis
155 acceleration was included in the slope-parallel momentum equations using the traditional approx-
156 imation.

157 The simulation shown in Figure 1 had a domain of $3\text{km} \times 3\text{km} \times 200\text{m}$ with $480 \times 480 \times 101$
158 uniform grid points. The simulation was initialized with uniform temperature, T , and salinity, S ,
159 to match the far-field values from the Larsen C Ice Shelf observations. The initial slope-parallel
160 velocities are set to the velocities expected from the tidal forcing. Importantly, the initial T , S , and
161 velocity were spatially constant (aside from some small amplitude random noise). By comparing
162 the subsequent model T/S profiles with the observations, we were able to test whether the observed
163 bulk boundary layer properties could be reproduced by the local turbulence and melting. This
164 set-up in the relatively large domain allowed study of the turbulence evolution over several spring-
165 neap cycles in simulations lasting for over 100 days. To study the influence of model resolution
166 and the role of small-scale turbulence, another simulation was conducted in a smaller domain
167 $600\text{m} \times 200\text{m} \times 200\text{m}$ with $384 \times 128 \times 401$ uniform grid points. This domain was designed
168 to be orientated roughly along the tidal ellipses of the diurnal tides, O1 and K1 (more details in
169 Section 3c).

170 The entire evolution of the simulations was of interest, but we particularly focused on the in-
171 terval where the vertical gradient of the temperature and salinity profiles most closely matched
172 the observations. This was to ensure that the depths of the mixed layer and the stratified region
173 were similar in the simulations and observations. The simulations were an initial value problem

174 as there was no source of restoring heat and salinity, meaning that the boundary layer continued
 175 to freshen and cool and there was no long-term equilibrated state. Of course, it is unlikely that the
 176 small-scale flow under a melting ice shelf is in an unchanging equilibrated state either (e.g. syn-
 177 optic and seasonal variability is expected). It is worth noting that the simulations do not attempt
 178 to include any large-scale horizontal gradients in T , S that may be of importance in maintaining
 179 steady-state conditions (Jenkins 2016, 2021). The remainder of this section outlines further details
 180 of the numerical simulations.

181 *a. Numerical simulation setup*

182 The simulations solved the incompressible Navier-Stokes momentum equation (with the Boussi-
 183 nesq approximation), the conservation of mass, heat and salt and a linear equation of state,

$$\frac{D\mathbf{u}}{Dt} = -\frac{1}{\rho_0}\nabla p + \nu\nabla^2\mathbf{u} + \mathbf{F} - \frac{\Delta\rho}{\rho_0}g(\sin\theta\mathbf{i} + \cos\theta\mathbf{k}) - f\mathbf{k} \times \mathbf{u} - \nabla \cdot \boldsymbol{\tau}, \quad (4)$$

$$\nabla \cdot \mathbf{u} = 0, \quad \frac{DT}{Dt} = \kappa_T \nabla^2 T - \nabla \cdot \boldsymbol{\lambda}_T, \quad \frac{DS}{Dt} = \kappa_S \nabla^2 S - \nabla \cdot \boldsymbol{\lambda}_S, \quad (5)$$

$$\frac{\Delta\rho}{\rho_0} = -\alpha(T - T_0) + \beta(S - S_0). \quad (6)$$

186 where $\mathbf{u} = (u, v, w)$ was the velocity vector, (x, y, z) was the position vector, \mathbf{i} and \mathbf{k} were the unit
 187 vectors in the x and z directions respectively, t was time, p was pressure, T was temperature, S
 188 was salinity and ρ was density. The ice base slope was specified in the x -direction. The reference
 189 values of temperature, salinity and density were T_0 , S_0 and ρ_0 respectively, and $\Delta\rho = \rho - \rho_0$. The
 190 gravitational acceleration was $g = 9.81 \text{ ms}^{-2}$ and the slope away from the horizontal was $\theta = 0.5^\circ$.
 191 The coefficients of thermal expansion and saline contraction were $\alpha = 3.28 \times 10^{-5} \text{ }^\circ\text{C}^{-1}$ and $\beta =$
 192 $7.84 \times 10^{-4} \text{ psu}^{-1}$ respectively, which were chosen to be consistent with the ocean state beneath
 193 Larsen C Ice Shelf (Gibbs Seawater Oceanographic Toolbox, McDougall and Barker 2011). We
 194 used realistic values of the molecular viscosity $\nu = 1.8 \times 10^{-6} \text{ m}^2 \text{ s}^{-1}$ and the molecular diffusivity

195 of heat $\kappa_T = 1.3 \times 10^{-7} \text{m}^2 \text{s}^{-1}$ (Prandtl number $Pr = \nu / \kappa_T = 13.8$) and salt $\kappa_S = 7.4 \times 10^{-10} \text{m}^2 \text{s}^{-1}$
196 (Schmidt number $Sc = \nu / \kappa_S = 2432$). The Coriolis parameter was $f = -1.35 \times 10^{-4} \text{rad s}^{-1}$. The
197 tidal forcing $\mathbf{F} = (F_x \mathbf{i} + F_y \mathbf{j})$ includes the three dominant tidal constituents (O1, K1, and M2). As
198 described in Appendix A, the form of \mathbf{F} was set so that the far-field in the model velocity matches
199 the tidal ellipse and phase for each of the three constituents in the observations beneath Larsen C
200 reported in Davis and Nicholls (2019).

201 The sub-grid scale contributions to the momentum $\boldsymbol{\tau}$, heat $\boldsymbol{\lambda}_T$ and salt $\boldsymbol{\lambda}_S$ equations were calcu-
202 lated using the anisotropic minimum dissipation (AMD) model (Rozema et al. 2015; Abkar and
203 Moin 2017; Verstappen 2016). This sub-grid scale model was expected to work especially well in
204 the present simulations, which were strongly turbulent with relatively weak stratification (Vreug-
205 denhil and Taylor 2018). The AMD model was set up in the same manner as past simulations of
206 under ice shelf flow by Vreugdenhil and Taylor (2019).

207 Eqns. 4–6 were discretised into Fourier modes in the periodic slope-parallel directions and
208 with second order finite differences in the wall-bounded vertical direction (see Taylor 2008).
209 When moving from Fourier space to physical space, a 2/3 dealiasing rule was applied (Orszag
210 1971). The equations were solved with a low-storage third-order Runge–Kutta method and
211 a semi-implicit Crank–Nicholson method was used for the viscous and diffusive terms. The
212 Courant–Friedrichs–Lewy condition was used for the adaptive time-step.

213 *b. Near-wall model algorithm*

214 The LES resolution was too low to resolve turbulence close to the ice/ocean boundary where
215 the distance from the boundary limits the size of turbulent eddies. Instead, a near-wall model was
216 implemented to estimate the basal stress, melt rate, and heat and salt fluxes given the temperature,

217 salinity, and velocity at the top gridpoint of the computational domain. Details of the near-wall
218 model are in Appendix B, with key features described here.

219 The location of the uppermost computational gridpoint was placed in the law-of-the-wall loga-
220 rithmic layer where Monin–Obukhov scaling was expected to hold (Vreugdenhil and Taylor 2019).
221 Observations beneath Larsen C Ice Shelf suggested that the logarithmic layer extended to at least
222 2.5m in depth (Davis and Nicholls 2019). In our LES, the first grid point was placed at 1m in the
223 large domain case and 0.25m in the small domain case. A smooth ice base formulation was chosen
224 as the roughness inferred from Davis and Nicholls (2019) was small. The near-wall model used
225 Monin–Obukhov scaling coupled with the diffusive melt equations (McPhee et al. 1987; Holland
226 and Jenkins 1999) to solve for the fluxes of heat, salt and momentum at the ice base. The near-wall
227 model was verified against past LES of the logarithmic layer that resolved the viscous sublayer (re-
228 solved LES from Vreugdenhil and Taylor 2019). The near-wall model is expected to work well
229 for the strongly turbulent and weakly stratified ocean beneath Larsen C Ice Shelf. If stratification
230 dominates the flow, as may be the case beneath George VI Ice Shelf for example (Kimura et al.
231 2015), the near-wall model may not be appropriate. The melt rate from the near-wall model was
232 updated each time step and had spatial dependence, as shown in Figure 1 for the Larsen C Ice
233 Shelf simulation.

234 Compared to the three-equation model (Eqns. 1–3) the advantage of the near-wall model algo-
235 rithm is that it does not assume constant values of the drag, heat and salt transfer coefficients (C_d ,
236 Γ_T and Γ_S). For an under-ice flow whose turbulence level does not vary significantly (zero or very
237 weak stabilising stratification) the three-equation model will do a reasonable job of modelling the
238 flow, provided that the correct values of C_d , Γ_T and Γ_S are chosen. Note that, even without stabil-
239 ising stratification, if the turbulence level varies significantly then a varying drag coefficient may
240 be required to accurately model the flow at different times (see fundamental turbulence review in

241 Pope 2000). Beneath Larsen C Ice Shelf there were large fluctuations in the ocean turbulence due
242 to the tides, with the additional complication of stabilising stratification due to melting (Davis and
243 Nicholls 2019). From the outset it was unclear how turbulence and stratification would interact
244 during the tidal cycle and impact the melt rate, which could have feedback effects on the water
245 column stratification and turbulence itself. Here we avoided making assumptions about C_d , Γ_T
246 and Γ_S but rather calculated them using the near-wall model algorithm.

247 3. Results

248 *a. Bulk properties of the flow*

249 The simulated flow beneath Larsen C Ice Shelf was initialised with uniform temperature, salinity
250 and tidal velocities. The strong tidal forcing followed a spring-neap cycle that appears clearly in
251 the bulk velocities (Figure 2a). The tidal cycle was also a key factor setting the friction velocity,

$$u_* = \sqrt{\tau/\rho_0}, \quad (7)$$

252 which is a measure of the strength of the stress, τ , at the ice base. As shown in Figure 2b, faster
253 tidal velocities resulted in a larger stress at the ice base and hence a larger friction velocity. Strong
254 turbulence during spring phases of the tidal cycle mixed heat towards the ice base, enhancing the
255 melt rate (Figure 2c). The melting ice base freshened and cooled the upper water column, creating
256 a mixed layer that deepened throughout the simulation (Figure 2d). The mixed layer depth was
257 measured as the depth at which the density was equal to $\rho_{top} + 0.01 \text{ kg/m}^3$. To put this in context,
258 the top-to-bottom density difference was 0.04 kg/m^3 (at Day 70). Since the melt rate was depen-
259 dent on the temperature and salinity in the near-ice region, and since there were periodic boundary
260 conditions in the directions parallel to the ice base, over time the melt rate slowly decreased as

261 the mixed layer became fresher and colder. The melt rate from field observations (0.7m/yr) is
262 consistent with the initial melt rate diagnosed in the LES.

263 The deepening mixed layer is also shown in the evolving temperature and salinity profiles (Fig-
264 ure 3a,b). Despite initialising the model with uniform T and S , the profiles around Day 70 compare
265 reasonably well with the observed CTD profiles, in particular when considering the vertical gra-
266 dient profiles (Figure 3c,d). It is worth noting that the model is colder and fresher in the mixed
267 layer at the times when the gradient profiles most closely match. Nevertheless, the overall shape
268 of the profiles is similar to observations with a well-mixed region immediately beneath the ice
269 base, followed by stratification, and then the far-field region as yet unaffected by the local melting
270 ice. This shows that the basic vertical structure in the CTD profiles can be generated through local
271 production of meltwater and vertical mixing.

272 On the T - S diagram (Figure 3e), the initial uniform T , S are represented by a single point at
273 $T = -1.955^{\circ}\text{C}$ and $S = 34.57$ psu. As time progressed, the upper water column freshened and
274 cooled and the profiles extended towards the T - S freezing point line (dotted line on Figure 3e).
275 The T - S slope is consistent with the first set of CTD observations (dark green), except near the
276 ice base where the observed profile diverged, possibly due to brine rejection from re-freezing near
277 the hot-water drilled borehole. The latter set of CTD observations (light green) was only taken 7
278 hours later but shows a shift in T - S angle which was not seen in the LES. This is a clear indication
279 of lateral advection across the observation site, where the advected waters could be influenced by
280 ice melting into a different “source water”, something the model cannot be expected to capture
281 because of the periodic boundary conditions.

282 To compare with the DN19 observations, the covariance method was used to estimate the friction
 283 velocity by using Reynolds stresses at different depths,

$$u_*^{covar} = [(u'w')^2 + (v'w')^2]^{1/4}, \quad (8)$$

284 where the LES u_*^{covar} included both the resolved and sub-grid scale contributions. The dash indi-
 285 cates deviation from the mean, where the LES used the slope-parallel mean and the observations
 286 used the burst-averaged time mean (the observations were taken for 15 minute bursts every two
 287 hours). In Figure 4a the friction velocity calculated using the covariance method (Eqn. 8) from the
 288 LES is compared with the DN19 observations. The chosen depths, 2.5m and 13.5m, corresponded
 289 to the two velocity instruments in the field observations referred to as the Upper and Lower Mod-
 290 ular Acoustic Velocity Sensor (MAVS) respectively. To put this in perspective, the depth of the
 291 Ekman layer (which was set up within the first 12 hour period) was roughly $\sqrt{2\nu_{SGS}/f} = 3.8\text{m}$,
 292 where $\nu_{SGS} \approx 10^{-3} \text{ m}^2\text{s}^{-1}$ was the maximum turbulent viscosity. While the LES has generally
 293 smaller covariance friction velocities, the trend was the same as the DN19 observations with the
 294 Upper MAVS having a stronger friction velocity than the Lower MAVS. The smaller friction ve-
 295 locities in the LES might be due to smooth ice assumed in the near-wall model, but could also
 296 be due to turbulence from other sources that were not present in the idealized simulations (further
 297 discussion in Section 4).

298 The drag coefficient, $C_d^{covar} = (u_*^{covar}/U)^2$, increased at low flow speeds in both the LES and
 299 Upper MAVS observations as shown in Figure 4b. For the Upper MAVS, DN19 attributed this to
 300 the instrument moving into and out of the logarithmic layer. A different explanation emerges after
 301 considering the LES evolution in Figure 4c. The tidal current (grey dashed line) drove the main
 302 flow, with the friction velocity at the ice base (orange line) following closely. The shear turbulence
 303 generated at the ice-base then took time to propagate to depth, resulting in an offset for u_*^{covar}

304 measured at depth as shown for Day 76 in Figure 4d. The tidal current with depth is also included
305 for Day 76 in Figure 4e. One reason for the time offset is that the weak stratification in the mixed
306 layer needed to be eroded away by the turbulence as it propagated to depth, as shown for Day
307 76 in Figure 4f. So when the current speed U dropped towards zero, there was still turbulence at
308 depth so u_*^{covar} was still large, and C_d^{covar} increased. By the time the turbulence and u_*^{covar} started to
309 decrease, the current speed had increased again, and C_d^{covar} decreased. This explains the increase
310 in C_d^{covar} at small current speeds when C_d^{covar} was calculated using the current speed far from the
311 ice base. This explanation is also consistent with the hysteresis shown in Figure 4a, b. Overall, the
312 u_*^{covar} at depth were smaller than u_* calculated at the ice base as shown in Figure 4c. The u_*^{covar}
313 also decreased further from the ice base, as less turbulence managed to propagate to these depths.

314 The ice base melt rate is strongly tied to the current speed as shown in Figure 5a. The chosen
315 depths for the current speed comparison were 2.5m and 13.5m (corresponding to the MAVS) along
316 with a notional far-field depth at 190m. For faster current speeds there was more turbulence near
317 the ice, larger friction velocity u_* (Figure 5b) and hence more melting. However, the melt rate
318 and u_* are not unique functions of the far-field speed (cyan lines) but exhibited an asymmetric
319 response to the tidal cycle, where the period of each loop corresponds to a single M2 tidal cycle.
320 These (cyan) loops are also slightly offset compared to the upper water column results (red and
321 blue lines). This offset can be explained by the presence of a buoyant meltwater plume. The
322 meltwater was relatively less dense and formed an upslope buoyant plume that ended up being
323 diverted to mainly across slope movement due to geostrophy (Jenkins 2016). Evidence for the
324 meltwater plume is most clearly shown by comparing flow velocities between simulations with
325 and without the ice base slope (Figure C1 in Appendix C). The meltwater plume has some velocity
326 in the upper region, which led to an offset in the response of the melt rate and u_* to changes in the
327 far-field current (compare Figure 5a with Figure C2 in Appendix C). When the buoyant current is

328 in the same direction as the tidal current, the current speed and melt rate are enhanced, and when
 329 they are in opposite directions the current speed and melt rate are suppressed.

330 The LES can help to determine whether setting single constant values of the transfer coefficients
 331 in the three-equation model is appropriate. The heat and salt transfer coefficients in Figure 5d,e
 332 were calculated as

$$\Gamma_T = \frac{\kappa_T |\frac{\partial T}{\partial z}|_b}{u_*(T - T_b)}, \quad \Gamma_S = \frac{\kappa_S |\frac{\partial S}{\partial z}|_b}{u_*(S - S_b)}, \quad (9)$$

333 where $|\partial T/\partial z|_b$ and $|\partial S/\partial z|_b$ are, respectively, the diffusive heat and salt fluxes across the ice-
 334 ocean boundary. For different depths, the only parameters in Eqn. 9 that changed were T and S
 335 and the remaining values were obtained from the near-wall model (Eqns. 9 are re-written from
 336 Eqns. B14 in Appendix B). The mixed layer gave Γ_T , Γ_S similar to those inferred from observa-
 337 tions beneath Ronne Ice Shelf of $\Gamma_T = 0.011$ and $\Gamma_S = 3.1 \times 10^{-4}$ (Jenkins et al. 2010). When
 338 comparing the results from the upper mixed layer to the far-field, the depth dependence of Γ_T is
 339 particularly strong. Transfer coefficients for the three-equation model did not vary significantly
 340 when the chosen depth of input values was within the top 15 m of the mixed layer, but the concept
 341 of depth-independent transfer coefficients fails when applied to the far-field values below the py-
 342 cnocline. This result was not surprising as the three-equation model was formulated to work with
 343 values up to the outer edge of the boundary layer. The three-equation model was not designed
 344 to parameterize mixing through the pycnocline and, from the simulations shown here, we caution
 345 that it should not be used beyond the boundary layer (in this case the mixed layer).

346 In Figure 5c, the drag coefficient using friction velocity calculated at the ice base, $C_d = (u_*/U)^2$,
 347 is plotted against speed at the three depths. The drag coefficient calculated with the ice base friction
 348 velocity C_d did not vary much with flow speed at 2.5m depth, with more variance at 13.5m depth
 349 and in the far-field. This is also demonstrated in the vertical profiles of C_d in Figure 5f. The LES
 350 shows that the drag coefficient was a quite well defined quantity within the mixed layer, as long

351 as the interfacial stress is used. In contrast, the covariance drag coefficient C_d^{covar} (Figure 4b) does
352 not tend as nicely to a single value, especially if the measurement was made further from the ice
353 base. In other words, the interfacial stress is not well represented by the covariance-calculated
354 stress, especially far from the ice (13.5m or deeper). This is because, fundamentally, it is not a
355 constant stress boundary layer.

356 Observations are unable to make any direct measurement of the shear stress at the ice/ocean
357 interface. Even borehole observations like DN19 are limited to estimating the shear stress from
358 measurements a few metres from the ice base. Instead the basal stress is commonly inferred by
359 assuming that the measured velocity some distance from the ice is related to the friction velocity
360 through a constant drag coefficient. Our LES show that it might be acceptable to use a constant
361 value of C_d in models that resolve the mixed layer, although the drag coefficient does vary (by up
362 to an order of magnitude) at very low flow speeds.

363 *b. Ekman rolls*

364 The simulated flow had significant structure at scales of 100m-1km in the ice slope-parallel
365 directions, despite the fact that the computational domain was homogeneous in these directions.
366 Figure 6 shows elongated features in the slope-parallel speed at 20m depth, with associated upward
367 and downward motions. A signature of these features also appears in temperature and salinity as
368 undulations in the stratification. Since the departure from the plane-averaged velocity forms closed
369 circulation cells, we refer to these features as ‘rolls’, although note that the isopycnals associated
370 with these features do not overturn and hence these features could instead be referred to as ‘waves’.

371 These features qualitatively match the description of roll-like structures that emerge following
372 linear instabilities in Ekman layer velocity profiles (Lilly 1966; Faller and Kaylor 1966; Brown
373 1972; Deusebio et al. 2014; Mkhinini et al. 2013). In laboratory experiments and simulations

374 of steady, unstratified flow the Ekman rolls remained almost stationary with and parallel to the
375 imposed current (Lilly 1966; Faller and Kaylor 1966). Strong stabilising stratification can turn
376 the angle of the Ekman rolls further from the imposed current orientation and allow the rolls to
377 propagate with the imposed current (Brown 1972).

378 In the LES here, there was weak stabilising stratification from ice melting and strong oscillating
379 flow from the tides. The Ekman rolls appeared to be mainly stationary in angle but were translated
380 in the slope-parallel directions (back and forth) by the changing tide. The Ekman rolls were not
381 always present in time, generally forming at the weaker currents in the spring-neap tidal cycle. For
382 stronger currents, especially when there was a rapid change in current direction, there was more
383 turbulence and Ekman rolls were no longer a strong feature. In the remainder of this section we
384 investigate these Ekman rolls more quantitatively.

385 The energy in the rolls can be quantified by calculating the turbulent kinetic energy (TKE)
386 in wavenumber space. The Ekman rolls exhibited significant 2D structure in the slope-parallel
387 directions, hence a 2D slice at 20m depth was chosen to investigate the rolls in wavenumber space,
388 as shown in Figure 7 for Day 70. The TKE maximum resided in wavenumbers consistent with the
389 Ekman roll structures in Figure 6, corresponding to dimensionless wavenumbers $kL/2\pi = 3$ and
390 $lW/2\pi = 5$ for Day 70, where k and l are the dimensional wavenumbers and L and W are the
391 domain sizes in the x and y directions respectively. In order to examine the size and orientation of
392 the rolls, we chose a minimum value of the TKE to define a cut-off envelope. For values within the
393 envelope, the wavenumbers were weighted by the TKE to find the average k and l wavenumbers
394 associated with the rolls. The cut-off TKE was chosen as $3 \times 10^{-9} \text{ m}^2\text{s}^{-2}$, which encompassed the
395 majority of the TKE peak (green contour in Figure 7). A sensitivity analysis was conducted to find
396 the best cut-off TKE to capture the TKE peak without including contributions from wavenumbers
397 that were clearly outside the region of interest. The TKE cut off was applied in wavenumber space

398 to each time, meaning that the green contour varied somewhat in wavenumber space over time,
399 but it was noted to capture the roll activity for the majority of the simulation.

400 The resulting width and angle of the Ekman rolls over time are shown in Figure 8b,c. The
401 angle was defined with respect to the x -direction (the direction of ice base slope) and describes the
402 longitudinal direction of the rolls (i.e. perpendicular to the periodicity in the structures). Figure 8a
403 includes the mean speed at the same depth ($z = -20\text{m}$) to illustrate the timing of the tidal cycle.
404 The roll structures are clearly visible by Day 10, where they were approximately 200m wide and at
405 an angle of 60° , so significantly smaller than the domain size (3km). As the simulation progressed,
406 the rolls widened while the roll angle stayed about the same. The rolls were aligned roughly
407 parallel to the diurnal tidal ellipse maxima (K1 and O1). This was consistent with linear stability
408 theory in which the Ekman rolls aligned parallel to the driving current (Lilly 1966). Interestingly,
409 when the basal slope was not present, the roll width remained around 200m for almost the entire
410 simulation (Appendix C). The mixed layer depth grew at a similar rate regardless of the basal slope
411 and meltwater plume presence (not shown here). This implies that the widening of the Ekman
412 rolls could be the result of some other interaction with the meltwater plume. In other words, even
413 though the stratification was similar between simulations with and without ice base slope, in the
414 former case the meltwater could drive flow and hence change the shear and Ekman roll width.

415 The cut-off envelope was also used to calculate the fraction of the total TKE associated with the
416 rolls (Figure 8d). The rolls were responsible for more than half of the total TKE at all times. In
417 general, the rolls were less well defined (a smaller fraction of the TKE) during times with a strong
418 tidal current. This could be due to more shear turbulence at the large flow speeds (especially when
419 there was a sudden change in speed) resulting in the break-up of the rolls.

420 *c. Turbulence*

421 The influence of small-scale turbulence on the vertical heat flux and melt rate will now be in-
422 vestigated using the high resolution simulation in the small domain where more of the small-scale
423 turbulence was directly resolved. This simulation also provided a test of the resolution depen-
424 dence of the LES results. The relatively large Ekman rolls presented a challenge when setting up
425 the simulation in a small domain with periodic boundary conditions. To overcome this challenge,
426 the small computational domain (x', y', z) was aligned with the dominant angle of the Ekman
427 rolls, as shown in Figure 6. The small domain could therefore capture one 600m wide Ekman roll
428 based on the roll width at Day 52 in the large domain simulation. To reduce the computational
429 cost, a smaller domain size of 200m was used in the direction parallel to the Ekman rolls. The
430 small domain simulation was initialised from mean profiles taken at Day 52 of the large domain
431 simulation (interpolated onto the finer grid). For comparison, an additional simulation of the large
432 domain was also initialised from mean profiles taken at Day 52: this will be the large domain (low
433 resolution) simulation used for all comparisons in this subsection. The small domain simulation,
434 along with the reinitialised large domain simulation, were run for 30 days.

435 The three-dimensional snapshot at Day 70 in Figure 9 shows that the rolls clearly aligned with
436 the domain, but rather than one 600m wide roll, there were three 200m wide rolls. One explana-
437 tion was that the Ekman rolls first form through an instability at the wavenumber corresponding
438 to 200m. The rolls remained 200m wide in the small domain simulation. In comparison, the
439 reinitialised large domain simulation also formed 200m wide rolls until Day 68 where they grew
440 in size to around 600m (not shown here). This suggests that the size of the Ekman rolls might
441 be sensitive to the time history of the flow and the larger scale motions not captured in the small
442 domain. Figure 9 also shows a layer of small-scale turbulence immediately beneath the ice base.

443 The majority of the mixed layer heat flux in the small domain simulation was due to resolved
444 turbulence. Figure 10 shows vertical profiles of the subgrid-scale (SGS) diffusivity, κ_{SGS} , (panel
445 a) and of the resolved and SGS components of the heat flux for the large (panel b) and small (panel
446 c) domain simulations. In the small domain simulation, κ_{SGS} was roughly a quarter of that in the
447 large domain case (Figure 10a). The chosen SGS model (the anisotropic minimum-dissipation
448 model) calculated κ_{SGS} for each grid cell and time step using the three-dimensional velocity and
449 temperature fields. Smaller values of κ_{SGS} meant that the resulting SGS contribution to the total
450 vertical heat flux was reduced for the small domain simulation (Figures 10b, c). Interestingly, the
451 resolved heat flux contribution was only a little larger for the small domain simulation. For the
452 large domain simulation, the heat flux was strongly dominated by the SGS contribution, leading to
453 a large total heat flux. As the small domain simulation saw a big decrease in the SGS contribution
454 and only a small increase in the resolved portion, this lead to an overall reduction in the total heat
455 flux compared to the large domain simulation, which will be explored further later in this section.

456 Continuing with the analysis of the small domain simulation, the time evolution of total TKE
457 and heat transport associated with flow at different depths (10m and 20m), along with the roll
458 contribution, is shown in Figure 11. The TKE and vertical heat flux were calculated using a 2D x' -
459 direction slice of velocities and temperature for each depth in wavenumber-depth space (not shown
460 here). In wavenumber-depth space, the TKE was strongest at wavenumber $k'L/2\pi = 3$ (consistent
461 with the three Ekman rolls in Figure 9) and the depth of maximum TKE fluctuated between 20m
462 to 30m with the changing tidal currents. The partitioning into the roll contribution in Figure 11
463 used the TKE cutoff of $6 \times 10^{-6} \text{ m}^2\text{s}^{-2}$, which was equivalent to the TKE cutoff used in Figures
464 7 and 8 for the large domain simulation but re-normalised for the small domain dimensions.

465 The resulting TKE evolution shows a time offset between 10m and 20m depth (Figure 11b,d).
466 At 10m there was an envelope of larger TKE (less than half of which lies with the Ekman rolls)

467 that matched the timing of the driving tidal forcing, though with a slight lag from the far-field flow
468 (Figure 11a). This is consistent with the fluctuations at 10m being shear turbulence associated with
469 the tidal forcing. For the 20m depth, the envelope with larger TKE occurred after the maximum
470 tidal forcing and was almost entirely associated with the Ekman rolls. The timing of the Ekman
471 rolls at 20m depth is consistent with the timing of the roll component of the TKE at 10m depth,
472 meaning that it was the rolls that lagged the tidal envelope. There was more total heat flux at
473 10m (Figure 11c,e), which matches the time-averaged depth profiles of heat flux contributions in
474 Figure 10 (recall that the total heat flux was comprised of the resolved plus the sub-grid scale
475 contributions). The Ekman rolls were responsible for only a tiny portion of the total heat flux,
476 both at 10m and 20m, as shown in the cumulative sum of heat flux in Figure 11f. The implication
477 is then that the heat flux was dominated by higher wavenumbers, so smaller physical scales. Even
478 though Ekman rolls contributed strongly to the TKE, they were only directly responsible for a
479 small amount of vertical heat transport. Of course, the rolls could still be important for the heat
480 transport in a more indirect manner, for example by driving smaller scale features that then mix
481 the heat vertically. But so far there is no clear link between the rolls and the vertical heat transport.

482 For the small domain simulation, the vertical profiles of T/S show that the upper water column
483 became more well mixed while the stratification below tended to sharpen (Figure 12). Interest-
484 ingly, the small domain (high resolution) simulation did not match the Larsen C Ice Shelf observed
485 profiles as well as the large domain (low resolution) simulation. This could be indicative of ad-
486 ditional processes that have not been explicitly included in the simulations (further discussion in
487 Section 4). The melt rate was smaller for the small domain simulation (0.136 m/yr time-averaged
488 over Days 65-75) compared to the large domain simulation (0.280 m/yr time-averaged over Days
489 65-75). The mixed layer did not significantly deepen during the small domain simulation, while
490 the large domain simulation showed a deepening of the mixed layer (from 30m to 34m depth).

491 This was consistent with the previous results (such as Figure 10) that show a reduction in heat flux
492 towards the ice base in the small domain simulation.

493 In conclusion, the small domain simulation saw a modest increase in resolved heat transport due
494 to the higher resolution, but the total heat transport was reduced because of a smaller sub-grid scale
495 contribution. While the Ekman rolls were correlated with around half of the total turbulent kinetic
496 energy, they were not directly responsible for significant heat transport. Overall, the reduced
497 mixing in the small domain simulations resulted in less heat transport towards the ice base, a
498 stagnating mixed layer depth and a reduction in the melt rate.

499 **4. Discussion**

500 *a. Application of results to the ocean*

501 The Ekman rolls are robust features of the large-eddy simulations. To the authors' knowledge,
502 this is the first time that these features have been seen in simulations or observations of under ice
503 shelf flow. In observations, the Ekman rolls may be present but as yet unidentified. To predict how
504 the Ekman rolls signature may appear in borehole measurements, the large domain simulation
505 was sampled at a single point at 20m depth every 16 seconds and a wavelet analysis applied to
506 the resulting signal (Figure 13). There was a likely signature of Ekman rolls in the temperature
507 wavelet analysis with a period of about one hour, consistent to intervals where the Ekman rolls
508 were observed in the 3D flow field. This period corresponded to the movement of a roll through
509 the measurement location. This was heavily dependent on the tidal current speed, but for intervals
510 when the tidal current was mostly in one direction for 12 hours or so there was a corresponding
511 increase in the Ekman roll signature. This signature also clearly appeared in the velocity wavelet

512 analysis (not shown here). Unfortunately this period was not sampled in the DN19 observations,
513 but in the future, it might be possible to identify Ekman rolls with a different sampling strategy.

514 In the ocean there are other sources of variability that may not be present in the LES. The
515 small domain simulation produced temperature and salinity profiles, and a melt rate, that were
516 further away from the observations than the large domain results. The rapid cooling and lack of
517 stratification in the mixed layer in the small domain simulation suggests that the heat in the mixed
518 layer was consumed too rapidly relative to its supply. This then implies that there was a supply
519 of heat to the mixed layer that was missing: either vertical mixing being too weak or an absence
520 of lateral heat advection. There is evidence that lateral advection was present in the observations
521 (discussed further below) so it is likely at least part of the explanation for the additional supply of
522 heat to the mixed layer. A lack of mixing may also be involved, but it is unclear how great a role
523 it will have played. Below we discuss the potential differences between the LES and real ocean.

524 One difference between the LES and the ocean was the periodic nature of the simulations in
525 the directions parallel to the ice base. The real-world ocean is not periodic. Neighbouring water
526 masses may differ significantly and could feasibly be moved into the domain at different stages
527 of the tidal cycle. There was some evidence for this in the observations, where the T and S
528 profiles significantly cooled and freshened over a brief 7 hour interval (Figure 3). There also could
529 have been additional mixing as the neighbouring water mass was transported back and forth, in
530 particular between the far-field flow and the upper mixed layer. Along with different water masses
531 being advected with the tidal cycle, there could also be incoming plume flow from further down the
532 ice shelf. While the observations measure only a weak background flow, even a weak plume from
533 external sources may still have significantly different temperature and salinity than the idealised
534 LES. There is more work to be done to quantify the heat transport from plumes and neighbouring
535 currents and how they might impact the stratification of the water column.

536 Next we consider whether the near-wall model might be responsible for discrepancies in strati-
537 fication between the simulations and observations. The ice base roughness parameter in the LES
538 was effectively set to zero in the near-wall model. As outlined in Appendix B, the Larsen C
539 Ice Shelf observations may have been in a transitionally rough regime. In this regime the ice base
540 roughness may or may not have had some influence on the flow depending on the roughness shape,
541 alignment and other characteristics (Jiménez 2004). Even so, the roughness length scale of 0.4mm
542 inferred from observations was still relatively minor and not too dissimilar from the smooth ice
543 base in the simulations. There is a caveat that the results from the present simulations demonstrate
544 that the observations may be underestimating (by approximately 25%) the true interfacial stress
545 on which the roughness calculation is based, so the true roughness could be somewhat larger.
546 However, even if the roughness were explicitly included in the near-wall parameterization, the ad-
547 ditional turbulence and mixing would be close to the ice base, rather than through the pycnocline
548 where more mixing could transport heat upwards into the mixed layer. The small difference in the
549 roughness parameter between the LES and observations is likely not sufficient to explain the lack
550 of heat within the mixed layer (seen in the small domain simulation).

551 Another explanation for the difference between the small domain LES and the observations is
552 that there may be other sources of mixing that have not been included in the LES. One example is
553 double-diffusive effects due to the large difference in molecular diffusivities between temperature
554 and salinity. There was a faint signature of steps in the observed T/S profiles (30-80m depth),
555 which may be indicative of double-diffusive layering, where small-scale diffusion across the layer
556 could drive mixing within the layers. The grid spacing of the LES would not have been able to
557 resolve double-diffusive layering, so any additional mixing from this source could explain the dif-
558 ference between the observations and the LES. There also could have been internal waves coming
559 from external sources, which would potentially break and mix regions of the water column be-

560 neath the ice base, but so far we do not have any evidence of internal waves breaking in the ocean
561 beneath Larsen C Ice Shelf. Investigating possible sources of mixing is another important area of
562 research at the frontier of ice shelf/ocean interactions.

563 *b. Three-equation model*

564 The ice shelf/ocean boundary parameterization of the three-equation model was also examined
565 here using the LES. The heat and salt transfer coefficients calculated with input T and S above the
566 pycnocline (upper 20m or so beneath the ice) showed almost no variation with flow speed. The
567 drag coefficient C_d calculated with the friction velocity at the ice base and flow speed at 2.5m depth
568 showed little variation with flow speed. Values of C_d with input flow speeds from 13.5m and below
569 showed more variation, particularly at low flow speeds. It is worth noting that the drag coefficient
570 might also be expected to vary through time as it is predicted to be a function of stability, and so it
571 may change with the melt rate (i.e. interfacial buoyancy flux). While this was not directly found
572 for Larsen C Ice Shelf here, it may be of importance for ice shelves with higher melt rates.

573 The LES results demonstrate that it may be acceptable to use the three-equation model with
574 constant coefficients (for Larsen C Ice Shelf or similar) if the first grid point is placed only a few
575 metres from the ice base. Beyond a few metres, the drag coefficient begins to vary more signifi-
576 cantly and may cause inaccurate modelling of the melt rate and other parameterized variables. A
577 coarser resolution ocean model using the three-equation model would likely place the first grid
578 point in the mixed layer region (i.e. interacting with the ice). However, a coarse resolution model
579 is likely to result in an effective mixed layer thickness that is too great with consequently biased
580 properties. Unfortunately, without knowledge of the modelled region, it is difficult to predict *a*
581 *priori* the depth of the mixed layer. In coarser ocean models (e.g. cavity sized models) the entire
582 near-ice region will require parameterization. Some regions of the cavity (e.g. near the grounding

583 line) may be affected by a strong geostrophic plume that drives the boundary layer flow, and in a
584 coarse model this is likely to be missed (Jenkins 2016, 2021; Patmore et al. in prep.). Additional
585 complications are likely to be present for different ice shelves, such as strong stratification, ice base
586 roughness or topography, a more vigorous meltwater plume, and double-diffusive convection.

587 **5. Conclusions**

588 The ocean-driven basal melting of Larsen C Ice Shelf was examined using large-eddy simula-
589 tions with realistic tides, ice base slope and Coriolis parameter. We used a new near-wall param-
590 eterization to calculate the ice shelf melt rate in the LES. The simulations matched reasonably
591 well with the observed stratification, friction velocity and time-averaged melt rate. One interest-
592 ing result was that the friction velocity estimated using the covariance method (typically used for
593 in-situ observations taken a few metres from the ice) had a time offset with depth and a reduced
594 magnitude with depth. This ultimately shows that the sub-ice upper mixed ocean was not a con-
595 stant stress boundary layer and that the turbulence generated at the ice base took some time to
596 propagate to depth. Additionally, the instantaneous melt rate was strongly tied to the tidal cycle,
597 which dominated the current speed within the mixed layer immediately beneath the ice.

598 The simulations also revealed Ekman rolls in the mixed layer and stratified region beneath
599 Larsen C Ice Shelf. While the bulk flow properties were dominated by the tidal forcing, the roll
600 behaviour was modified by the presence of the slope, with the roll width slowly increasing over
601 time. The Ekman rolls contributed noticeably to the turbulent kinetic energy but barely affected
602 the vertical heat transport directly. Hence questions remain on whether it is necessary to include
603 the effects of Ekman rolls in melt rate parameterizations such as the three-equation model.

604 In terms of the three-equation model, the heat and salt coefficients calculated using temperature
605 and salinity values within the mixed layer (top $\sim 20\text{m}$) were largely independent of current speed

606 and were consistent with past observations such as from Ronne Ice Shelf (Jenkins 2011). The drag
607 coefficient C_d at the ice base was nearly constant when considering current speeds close to the
608 ice base (2.5m depth), but varied significantly when calculated using the current speed below the
609 mixed layer, particularly during intervals with low flow speeds. The LES results caution the use of
610 the three-equation model, in particular with a constant drag coefficient, unless the vertical ocean
611 structure beneath the particular ice shelf site is known *a priori*.

612 Although our simulations captured some details of the observations, there were notable differ-
613 ences. In particular, the stratification at the base of the mixed layer in the high resolution simulation
614 was larger than observed, and the modeled melt rate in this case was smaller than the observations.
615 This suggests that some processes that are not captured in our simulations might be important
616 sources of heat transport. For example, our model setup does not include advection of large-scale
617 temperature and salinity gradients, double diffusion, or a background internal wave field. It is
618 possible that a more realistic model of the full ice-shelf cavity could provide additional insight,
619 in particular on the large-scale advection of water mass properties. Parameter sensitivity studies
620 would also be useful to predict how the results might change in time or differ at other locations.
621 Ultimately, however, additional observations will be needed to identify the processes that control
622 the melt rate. There remains significant work to improve our understanding of ice shelf/ocean
623 interactions and the rich dynamics in these regions.

624 *Acknowledgments.* The NERC Standard Grant NE/N009746/1 is gratefully acknowledged for
625 supporting this research. This work used the ARCHER U.K. National Supercomputing Service
626 (<http://www.archer.ac.uk>).

627 APPENDIX A

628 **Tidal forcing terms for the momentum equation**

629 The tidal forcing in the LES was based on the in-situ velocity observations taken below Larsen
630 C Ice Shelf by Davis and Nicholls (2019). The strongest tidal components from the observations at
631 13.5m depth were chosen (O1, K1, M2) and, by assuming geostrophic balance, a pressure gradient
632 force was calculated. There is a question about how truly geostrophic the velocities are at 13.5m
633 depth, which might lie within the mixed layer and be influenced by ice base friction and other
634 boundary dynamics. But as these data are the most comprehensive information available on the
635 Larsen C Ice Shelf tidal velocities, they are used to force the model.

636 To derive the tidal forcing F_x, F_y in Eqn. 4 we solved the time variant geostrophic equations,

$$\frac{du}{dt} - fv = F_x, \quad \frac{dv}{dt} + fu = F_y. \quad (\text{A1})$$

637 Re-writing F_x, F_y with the three chosen tidal components, $F_x = F_{x,O1} + F_{x,K1} + F_{x,M2}$ and $F_y =$
638 $F_{y,O1} + F_{y,K1} + F_{y,M2}$. Considering just the O1 tidal components, the u_{O1} and v_{O1} velocities are

$$u_{O1} = A_{u,O1} \cos(\omega_{O1} t_{tide} - \Phi_{u,O1}), \quad v_{O1} = A_{v,O1} \cos(\omega_{O1} t_{tide} - \Phi_{v,O1}), \quad (\text{A2})$$

639 where A is the amplitude, $\omega = 2\pi/T$ is the tidal frequency, T is the tidal period, and Φ is the
640 phase lag. The time $t_{tide} = t - t_{central}$ is relative to the central nodal time used to compute the ob-
641 served constituents which is approximately half a year, $t_{central} = 182.5 \text{ days} = 1.58 \times 10^7$ seconds.

642 Substitute Eqns. A2 into Eqns. A1 to find,

$$F_{x,O1} = -A_{u,O1} \omega_{O1} \sin(\omega_{O1} t_{tide} - \Phi_{u,O1}) - A_{v,O1} f \cos(\omega_{O1} t_{tide} - \Phi_{v,O1}), \quad (\text{A3})$$

$$F_{y,O1} = -A_{v,O1} \omega_{O1} \sin(\omega_{O1} t_{tide} - \Phi_{v,O1}) + A_{u,O1} f \cos(\omega_{O1} t_{tide} - \Phi_{u,O1}), \quad (\text{A4})$$

644 and $F_{x,K1}, F_{y,K1}, F_{x,M2}, F_{y,M2}$ follow the same form. The respective constants are based on val-
645 ues from Davis and Nicholls (2019), see Table 1. The strongest three measured tidal components
646 resulted in replicating important characteristics such as a regular spring-neap cycle, but did not
647 quite result in the same maximum amplitudes of speed that were sometimes present in the obser-

648 vations. To ensure that these maximum amplitudes were well represented in the simulations, a
 649 multiplication factor of 1.3 was used in the tidal forcing.

650 APPENDIX B

651 **Near-wall model for the ice melting boundary condition**

652 *a. Derivation of the near-wall model*

653 In order to derive the near-wall model algorithm, let us first review the Monin–Obukhov sim-
 654 ilarity theory for stratified flow. This theory relates the gradients in velocity, temperature and
 655 salinity by the common Monin–Obukhov functions Φ_m and Φ_s . In other words, the gradient pro-
 656 files are expected to be similar in shape. The Monin–Obukhov similarity equations for velocity,
 657 temperature and salinity are

$$\frac{\partial U}{\partial z} = \frac{u_*}{k_m z} \Phi_m(\xi), \quad \frac{\partial T}{\partial z} = \frac{T_*}{k_s z} \Phi_s(\xi), \quad \frac{\partial S}{\partial z} = \frac{S_*}{k_s z} \Phi_s(\xi), \quad (\text{B1})$$

658 where U is the speed, $u_* = \sqrt{\nu |\partial U / \partial z|_b}$, $T_* = \kappa_T |\partial T / \partial z|_b / u_*$ and $S_* = \kappa_S |\partial S / \partial z|_b / u_*$ are the
 659 friction velocity, temperature and salinity respectively. The subscript “b” indicates variables at the
 660 ice-ocean boundary. The von Kármán constants for the momentum and scalars are, respectively,
 661 $k_m = 0.41$ and $k_s = 0.48$ (Bradshaw and Huang 1995). The Monin–Obukhov functions Φ_m and Φ_s
 662 are functions of the normalised distance from the ice $\xi = z/L$. The Obukhov length,

$$L = -\frac{u_*^3}{k_m B}, \quad (\text{B2})$$

663 describes the relative strength of turbulence compared to stratification, where the vertical buoyancy
 664 flux at the ice-ocean interface is $B = g(\alpha \kappa_T |\partial T / \partial z|_b - \beta \kappa_S |\partial S / \partial z|_b)$. The Obukhov length can be
 665 thought of as the distance away from the ice, above which we might expect turbulence to dominate
 666 the flow, and below which the effects of stratification will be important.

667 To better understand these Monin–Obukhov functions, let us consider the case where the flow
668 has a very low interfacial buoyancy flux, which we refer to as a very weakly stratified case. If
669 stratification is very weak then the Obukhov length L becomes very large, and the normalised
670 distance from the wall ξ becomes small. As L is far from the wall, the majority of the flow is
671 unaffected by stratification and we would expect $\Phi_m = \Phi_s = 1$. This results in Eqn. B1 reverting
672 to the well known law-of-the-wall logarithmic scaling with no stratification term (Pope 2000).

673 If stratification is stronger then it can start affecting the turbulence in the flow. In particular,
674 we would expect strong stabilising stratification to damp out some or all of the shear turbulence.
675 The frictional Obukhov length $L^+ = L/(v/u_*)$ is one measure of the transition to turbulent flow.
676 When $L^+ > 200$ the flow is predicted to be fully turbulent. However, the form of the stratified
677 Monin–Obukhov function is still contested (e.g. Businger et al. 1971; Kaimal et al. 1976; Foken
678 2006). One straightforward and common form is of a linear function of ξ ,

$$\Phi_m(\xi) = 1 + \beta_m \xi, \quad \Phi_s(\xi) = 1 + \beta_s \xi, \quad (\text{B3})$$

679 where $\beta_m = 4.8$ and $\beta_s = 5.6$ are constants (Wyngaard 2010; Zhou et al. 2017). Here, we will use
680 the linear function Eqn. B3 to derive our near-wall model. By vertically integrating Eqn B1 we
681 find

$$\frac{U(z_g)}{u_*} = \frac{1}{k_m} \ln \left(\frac{z_g u_*}{v} \right) + \frac{\beta_m}{k_m} \xi(z_g) + 5, \quad (\text{B4})$$

$$\frac{T(z_g) - T_b}{T_*} = \frac{1}{k_m} \ln \left(\frac{z_g u_*}{v} \right) + \frac{\beta_m}{k_m} \xi(z_g) + (13Pr^{2/3} - 7.5), \quad (\text{B5})$$

$$\frac{S(z_g) - S_b}{S_*} = \frac{1}{k_m} \ln \left(\frac{z_g u_*}{v} \right) + \frac{\beta_m}{k_m} \xi(z_g) + (13Sc^{2/3} - 7.5), \quad (\text{B6})$$

684 where the final terms on the right hand side are integration constants that describe the thickness of
685 the viscous, heat diffusive and salt diffusive sublayers. These terms are set following past work on
686 boundary layer turbulence (Bradshaw and Huang 1995; Schlichting and Gersten 2003), stratified
687 plane Couette flow (Deusebio et al. 2015; Zhou et al. 2017) and ice melting studies (Kader and

688 Yaglom 1972; McPhee et al. 1987; Holland and Jenkins 1999; Vreugdenhil and Taylor 2019).
689 Note that we have evaluated the Eqns. B4–B6 for the input values of temperature, salinity and
690 velocity to be those in the first grid cell in the domain, designated by the depth subscript “g”.

691 A smooth ice base has been assumed by including the viscous length scale in the first term
692 on the RHS of Eqns. B4–B6, this could be replaced with a roughness length scale if there was
693 significant roughness on the ice base. In the DN19 Larsen C Ice Shelf observations the measured
694 drag coefficient was on average 0.0022 (for Upper MAVS flow at speeds $>0.1\text{m/s}$), which gave
695 a roughness length scale of 0.4mm. This roughness length scale is expected to be approximately
696 $1/30$ of the vertical amplitude of the roughness elements, which is then $k_r = 12\text{mm}$ (Jiménez
697 2004). A useful measure of the roughness effect on the flow is the roughness Reynolds number
698 $Re_r = k_r u_* / \nu$ (Jiménez 2004). The roughness Reynolds number for Larsen C Ice Shelf base is
699 $Re_r = 32$ (using $u_* = 0.0047\text{m/s}$ associated with $U = 0.1\text{m/s}$, and $\nu = 1.8 \times 10^{-6}\text{m}^2/\text{s}$). This places
700 the ice base in the transitional roughness regime (between approximately $4 < Re_r < 80$) where
701 roughness may start having an effect on the flow depending on the roughness shape, alignment
702 and other characteristics (Jiménez 2004). This minor roughness was not too dissimilar from the
703 smooth ice base in the simulations.

704 In past resolved LES the temperature, salinity and velocity profiles were well-described by
705 Monin–Obukhov similarity scaling for stratified flow (Eqns B4–B6), provided that the flow was
706 not too strongly stratified i.e. $L^+ > 200$ (Vreugdenhil and Taylor 2019). This is thought to be
707 the appropriate regime for the strongly turbulent and weakly stratified ocean beneath Larsen C Ice
708 Shelf.

709 Next we review the diffusive three-equation model for ice melting. The three equations are
710 the conservation of heat and salt across the ice-ocean boundary, and the liquidus condition which

711 describes the phase change of ice to liquid water, respectively,

$$c_w \rho_w u_* T_* = \rho_i L_i m, \quad (\text{B7})$$

712

$$\rho_w u_* S_* = \rho_i S_b m, \quad (\text{B8})$$

713

$$T_b = \lambda_1 S_b + \lambda_2 + \lambda_3 P, \quad (\text{B9})$$

714 where m is the melt rate, T_b and S_b are the temperature and salinity at the ice-ocean boundary
 715 (McPhee et al. 1987; Holland and Jenkins 1999). Recall that u_* is the interfacial momentum flux
 716 or friction velocity, and T_* and S_* are the interfacial heat and salt fluxes (normalised by the friction
 717 velocity). The subscript “w” refers to values for water and “i” for ice. The specific heat capacity
 718 for water is $c_w = 3974 \text{ J kg}^{-1} \text{ }^\circ\text{C}^{-1}$ and the latent heat of fusion is $L_i = 3.34 \times 10^5 \text{ J kg}^{-1}$. The
 719 coefficients in the linearised expression for the freezing point of seawater are $\lambda_1 = -5.73 \times 10^{-2}$
 720 $^\circ\text{C}$, $\lambda_2 = 8.32 \times 10^{-2} \text{ }^\circ\text{C}$ and $\lambda_3 = -7.53 \times 10^{-4} \text{ }^\circ\text{C dbar}$ (Jenkins 2011). Finally, the background
 721 pressure due to the ice depth $P = 304 \text{ dbar}$ is chosen to match Larsen C Ice Shelf. Following from
 722 previous studies using the diffusive three-equation model, we have assumed that the volume input
 723 of water due to ice melting, the salinity of ice and the conduction of heat through the ice are all
 724 zero (Gayen et al. 2016; Mondal et al. 2019; Vreugdenhil and Taylor 2019).

725 For our near-wall model we now have six equations (Eqns B4-B9) and six unknowns (u_* , T_* ,
 726 S_* , m , T_b , S_b) when driven by the external forcing conditions $T(z_g)$, $S(z_g)$ and $U(z_g)$. The equa-
 727 tions are solved using the multivariate Newton-Raphson iteration method. This method uses a first
 728 guess based on the previous time step, then with each iteration reduces the residual error, eventu-
 729 ally converging on a solution. The Newton-Raphson iteration method can become computationally
 730 expensive, depending on the number of iterations required for the solution to converge. To save
 731 on computer time, for each time step we solve Eqns B4-B9 with the slope-parallel averaged tem-
 732 perature $T(z_g)$, salinity $S(z_g)$ and speed $U(z_g)$ at the first grid cell inside the domain. This spatial

733 averaging follows from work on using the Monin–Obukhov scaling to parameterize the effects
734 of the atmospheric boundary layer (for example Moeng 1984). Once we have the solution for the
735 slope-parallel averaged values, for each boundary grid cell we scale the solution by the local values
736 of velocity, temperature and salinity. For the velocities the stress component is partitioned into the
737 streamwise and spanwise slope-parallel velocity components following Piomelli et al. (1989). We
738 note that our overall approach is similar to methods previously used for Monin–Obukhov similar-
739 ity theory applied to the atmospheric boundary layers for one scalar (temperature) (e.g. Businger
740 et al. 1971) which we have simply added in complexity in the form of two scalars (temperature
741 and salinity) that then have a complicated relationship through the diffusive three-equation model.
742 The resulting locally scaled solutions are

$$\tau_{13}(x, y, z = 0) = \frac{u(x, y, z_g)}{U(z_g)} \tau_w, \quad (\text{B10})$$

$$\tau_{23}(x, y, z = 0) = \frac{v(x, y, z_g)}{U(z_g)} \tau_w, \quad (\text{B11})$$

$$T_*(x, y, z = 0) = \frac{T(x, y, z_g) - T_b}{T(z_g) - T_b} T_*, \quad (\text{B12})$$

$$S_*(x, y, z = 0) = \frac{S(x, y, z_g) - S_b}{S(z_g) - S_b} S_*, \quad (\text{B13})$$

746 where $\tau_w = \rho_0 u_*^2$ is the wall shear stress. These can then be applied as flux boundary conditions in
747 the large-eddy simulations.

748 *b. Validation of the near-wall model*

749 The near-wall model was validated by comparing coarse resolution LES (with the near-wall
750 model) against resolved LES (which explicitly resolved the viscous and diffusive sublayers) from
751 Vreugdenhil and Taylor (2019). For both LES, the domain was the top 2m of the water column.
752 A constant pressure differential to drive flow and investigated two different pressure differentials

753 that resulted in two different friction velocities. A range of thermal driving $\Delta T = T_{z=-2m} - T_b$ was
 754 also covered. The coarse resolution LES had 8cm grid spacing in the vertical direction, which also
 755 determined the depth of the first grid point.

756 For the validation comparison, variables of interest are the heat Γ_T and salt Γ_S transfer coeffi-
 757 cients and the drag coefficient C_d calculated as

$$\Gamma_T = \frac{T_*}{T(z) - T_b}, \Gamma_S = \frac{S_*}{S(z) - S_b}, C_d = \left(\frac{u_*}{U(z)} \right)^2. \quad (\text{B14})$$

758 Written in this form, it is clear that there is a direct link between the transfer coefficient definition
 759 (Eqns. B14) and the Monin-Obukhov scaling (Eqns. B4). As the Monin-Obukhov scaling is a part
 760 of the near-wall model, it is instructive to determine whether the transfer coefficients (output from
 761 the near-wall model) deviate from the scaling significantly. Finally, the melt rate is also compared
 762 between the resolved and near-wall model simulations.

763 Figure B1 shows the resolved LES (closed symbols) compared with the near-wall model LES
 764 (open symbols). The values of $T(z)$, $S(z)$ and $U(z)$ were taken at depth $z = -2$ m (the domain
 765 depth) for the output shown in Figure B1. The model output could then also be compared with the
 766 Monin-Obukhov scaling, shown as the red lines in Figure B1 (where Eqns. B4 were calculated for
 767 $z = -2$ m rather than z_g). The Monin-Obukhov scaling remains dependent on u_* and so there are
 768 two red lines on Figures B1 a-c. The Figure B1d panel shows the thermal driving varying with melt
 769 rate, with the lines showing a theoretical limit on the melt rate for a “passive scalar” case where
 770 the gravity is turned off (more detail on the resolved LES in Vreugdenhil and Taylor (2019)).

771 Overall Figure B1 shows that the near-wall model performs well when the flow is turbulent (large
 772 L^+) and melt rate and thermal driving are weak. This is demonstrated by consistency between the
 773 heat, salt and momentum flux coefficients, along with the melt rate. When the thermal driving
 774 becomes strong the near-wall model salt transfer coefficient in particular begins to deviate from

775 the resolved LES (Figure B1b). This deviation is also where the resolved LES diverges from the
776 Monin-Obukhov scaling, whereas the near-wall model values remain consistent with the Monin-
777 Obukhov scaling. The latter result is perhaps unsurprising as the near-wall model is based on the
778 Monin-Obukhov scaling.

779 For the ocean boundary layer beneath the Larsen C Ice Shelf, Figure B2 shows the evolution
780 of the Obukhov length scale L^+ for the large domain near-wall model LES. For a large portion
781 of the spring-neap tidal cycle $L^+ > 10^3$, especially in the time interval that was of most interest
782 (Day 70 onwards). It was only for $L^+ < 10^3$ that there was significant departure for both Γ_T and
783 Γ_S (Figure B1). In the near-wall model LES, $L^+ < 10^3$ when the tidal forcing was weakest and
784 friction velocity smallest. These intervals are relatively short and, as both melt rate and friction
785 velocity were small here, we assume that the transfer coefficient departure did not significantly
786 influence the overall flow.

787 APPENDIX C

788 **Simulation without the slope and plume**

789 An additional large domain simulation was conducted with exactly the same set up as the original
790 sloped simulation (outlined in Section 2) but with no basal slope. The simulation was initialised
791 in the same manner and run for over 100 days. There was almost no change in most of the flow
792 properties examined here, with a couple of key exceptions outlined below.

793 The evolution of the slope-parallel velocity profiles is shown in Figure C1. The Ekman layer was
794 set up almost immediately (within the first 12 hour period) but continued to change over time as the
795 tides varied direction. The slow deepening of the mixed layer region is also shown in the velocity
796 profiles. The simulations with and without the basal slope showed flow that was quite similar,
797 but the sloped case showed more across-slope movement as there was a buoyant meltwater plume

798 (Figure C1). The buoyant plume is diverted to primarily across slope movement due to geostrophy
799 (Jenkins 2016).

800 The bulk properties of the stratification evolved in a very similar manner regardless of the basal
801 slope with minor influences on the bulk melt rate and friction velocities. One key difference
802 appeared when comparing the far-field speed to the instantaneous melt rate and drag coefficient
803 (Figure C2). There is noticeably less skewness in the histogram of C_d values at a given speed (cyan
804 lines) compared to the sloped simulation (Figure 5c). This is consistent with a weak meltwater
805 plume being present in the upper water column that has some distinct movement which is separate
806 from the tidal forcing movement in the far-field. The transfer coefficients Γ_T , Γ_S remain largely
807 unchanged.

808 The other main difference was the evolution of the Ekman rolls (Figure C3). The rolls formed in
809 the same manner as the sloped simulation, including the same angle and about 200m wide. Unlike
810 the sloped simulation, the roll width in the flat ice case remained at about 200m until the end of the
811 simulation, where the signal became weak compared to other flow turbulence. The cut-off TKE
812 then anomalously picked the domain-size as the dominant mode – this is an artefact of the method
813 for averaging TKE spectra if the overall signal becomes too weak. The roll contribution to the
814 total TKE was a similar contribution to the sloped case. The lack of a meltwater plume may be
815 the reason that the roll width remains close to 200m in the simulation with a flat ice base. We note
816 that the mixed layer depth appeared to continue evolving in depth with time, similar to the sloped
817 case, so this does not explain the limiting roll depth of 200m.

818 **References**

819 Abkar, M., and P. Moin, 2017: Large-eddy simulation of thermally stratified atmospheric
820 boundary-layer flow using a minimum dissipation model. *Boundary-Layer Meteorol.*, **165**, 405–

821 419, doi:<https://doi.org/10.1007/s10546-017-0288-4>.

822 Arzeno, I. B., R. C. Beardsley, R. Limeburner, B. Owens, L. Padman, S. R. Springer, C. L. Stewart,
823 and M. J. Williams, 2014: Ocean variability contributing to basal melt rate near the ice front of
824 Ross Ice Shelf, Antarctica. *Journal of Geophysical Research: Oceans*, **119** (7), 4214–4233.

825 Bathmann, U., V. Smetacek, H. de Baar, E. Fahrbach, and G. Krause, 1994: The expeditions
826 ANTARKTIS X/6-8 of the research vessel “POLARSTERN” in 1992/93. *Berichte zur Polar-*
827 *forschung (Reports on Polar Research)*, **135**, 236.

828 Begeman, C. B., and Coauthors, 2018: Ocean stratification and low melt rates at the Ross Ice Shelf
829 grounding zone. *Journal of Geophysical Research: Oceans*, **123** (10), 7438–7452.

830 Bradshaw, P., and G. P. Huang, 1995: The law of the wall in turbulent flow. *Proc. R. Soc. Lond. A*,
831 **451** (1941), 165–188.

832 Brown, R. A., 1972: On the inflection point instability of a stratified Ekman boundary layer.
833 *Journal of the Atmospheric Sciences*, **29** (5), 850–859.

834 Businger, J. A., J. C. Wyngaard, Y. Izumi, and E. F. Bradley, 1971: Flux-profile relationships in
835 the atmospheric surface layer. *Journal of the Atmospheric Sciences*, **28** (2), 181–189.

836 Darelius, E., I. Fer, and K. W. Nicholls, 2016: Observed vulnerability of filchner-ronne ice shelf
837 to wind-driven inflow of warm deep water. *Nature communications*, **7** (1), 1–7.

838 Davis, P. E. D., and K. W. Nicholls, 2019: Turbulence Observations Beneath Larsen C Ice Shelf,
839 Antarctica. *Journal of Geophysical Research: Oceans*, **124** (8), 5529–5550.

840 Deusebio, E., G. Brethouwer, P. Schlatter, and E. Lindborg, 2014: A numerical study of the un-
841 stratified and stratified ekman layer. *Journal of fluid mechanics*, **755**, 672–704.

- 842 Deusebio, E., C. P. Caulfield, and J. R. Taylor, 2015: The intermittency boundary in stratified
843 plane Couette flow. *J. Fluid Mech.*, **781**, 298–329.
- 844 Dinniman, M. S., X. S. Asay-Davis, B. K. Galton-Fenzi, P. R. Holland, A. Jenkins, and R. Tim-
845 mermann, 2016: Modeling ice shelf/ocean interaction in Antarctica: A review. *Oceanography*,
846 **29 (4)**, 144–153.
- 847 Faller, A. J., and R. E. Kaylor, 1966: A numerical study of the instability of the laminar Ekman
848 boundary layer. *Journal of the Atmospheric Sciences*, **23 (5)**, 466–480.
- 849 Foken, T., 2006: 50 years of the Monin–Obukhov similarity theory. *Boundary-Layer Meteorol.*,
850 **119 (3)**, 431–447.
- 851 Fretwell, P., and Coauthors, 2013: Bedmap2: improved ice bed, surface and thickness datasets for
852 Antarctica. *The Cryosphere*, **7 (1)**, 375–393.
- 853 Gayen, B., R. W. Griffiths, and R. C. Kerr, 2016: Simulation of convection at a vertical ice face
854 dissolving into saline water. *J. Fluid Mech.*, **798**, 284–298.
- 855 Hattermann, T., O. A. Nøst, J. M. Lilly, and L. H. Smedsrud, 2012: Two years of oceanic obser-
856 vations below the Fimbul Ice Shelf, Antarctica. *Geophysical Research Letters*, **39 (12)**.
- 857 Hellmer, H. H., F. Kauker, R. Timmermann, J. Determann, and J. Rae, 2012: Twenty-first-century
858 warming of a large antarctic ice-shelf cavity by a redirected coastal current. *Nature*, **485 (7397)**,
859 225–228.
- 860 Holland, D. M., and A. Jenkins, 1999: Modeling thermodynamic ice–ocean interactions at the
861 base of an ice shelf. *J. Phys. Oceanogr.*, **29 (8)**, 1787–1800.

- 862 Holland, P. R., T. J. Bracegirdle, P. Dutrieux, A. Jenkins, and E. J. Steig, 2019: West antarctic ice
863 loss influenced by internal climate variability and anthropogenic forcing. *Nature Geoscience*,
864 **12 (9)**, 718–724.
- 865 Jenkins, A., 1991: A one-dimensional model of ice shelf-ocean interaction. *Journal of Geophysi-
866 cal Research: Oceans*, **96 (C11)**, 20 671–20 677.
- 867 Jenkins, A., 2011: Convection-driven melting near the grounding lines of ice shelves and tidewater
868 glaciers. *J. Phys. Oceanogr.*, **41**, 2279–2294.
- 869 Jenkins, A., 2016: A simple model of the ice shelf–ocean boundary layer and current. *J. Phys.
870 Oceanogr.*, **46 (6)**, 1785–1803.
- 871 Jenkins, A., 2021: Shear, stability, and mixing within the ice shelf–ocean boundary current. *Jour-
872 nal of Physical Oceanography*, **51 (7)**, 2129–2148.
- 873 Jenkins, A., K. W. Nicholls, and H. F. J. Corr, 2010: Observation and Parameterization of Ablation
874 at the Base of Ronne Ice Shelf, Antarctica. *J. Phys. Oceanogr.*, **40**, 2298–2312.
- 875 Jenkins, A., D. Shoosmith, P. Dutrieux, S. Jacobs, T. W. Kim, S. H. Lee, H. K. Ha, and S. Stam-
876 merjohn, 2018: West antarctic ice sheet retreat in the amundsen sea driven by decadal oceanic
877 variability. *Nature Geoscience*, **11 (10)**, 733–738.
- 878 Jiménez, J., 2004: Turbulent flows over rough walls. *Annu. Rev. Fluid Mech.*, **36**, 173–196.
- 879 Kader, B., and A. Yaglom, 1972: Heat and mass transfer laws for fully turbulent wall flows.
880 *International Journal of Heat and Mass Transfer*, **15 (12)**, 2329–2351.
- 881 Kaimal, J., J. Wyngaard, D. Haugen, O. Coté, Y. Izumi, S. Caughey, and C. Readings, 1976:
882 Turbulence structure in the convective boundary layer. *Journal of the Atmospheric Sciences*,
883 **33 (11)**, 2152–2169.

884 Keitzl, T., J. P. Mellado, and D. Notz, 2016: Reconciling estimates of the ratio of heat and salt
885 fluxes at the ice-ocean interface. *Journal of Geophysical Research: Oceans*, **121** (12), 8419–
886 08 433.

887 Kimura, S., A. Jenkins, P. Dutrieux, A. Forryan, A. C. Naveira Garabato, and Y. Firing, 2016:
888 Ocean mixing beneath Pine Island glacier ice shelf, West Antarctica. *Journal of Geophysical*
889 *Research: Oceans*, **121** (12), 8496–8510.

890 Kimura, S., K. W. Nicholls, and E. Venables, 2015: Estimation of ice shelf melt rate in the presence
891 of a thermohaline staircase. *J. Phys. Oceanogr.*, **45**, 133–148.

892 Lilly, D. K., 1966: On the instability of Ekman boundary flow. *Journal of the Atmospheric Sci-*
893 *ences*, **23** (5), 481–494.

894 Lilly, J. M., 2017: Element analysis: a wavelet-based method for analysing time-localized events
895 in noisy time series. *Proceedings of the Royal Society A: Mathematical, Physical and Engineer-*
896 *ing Sciences*, **473** (2200), 20160 776.

897 Malyarenko, A., A. J. Wells, P. J. Langhorne, N. J. Robinson, M. J. Williams, and K. W. Nicholls,
898 2020: A synthesis of thermodynamic ablation at ice-ocean interfaces from theory, observations
899 and models. *Ocean Modelling*, 101692.

900 Martin, S., and P. Kauffman, 1977: An experimental and theoretical study of the turbulent and
901 laminar convection generated under a horizontal ice sheet floating on warm salty water. *J. Phys.*
902 *Oceanogr.*, **7** (2), 272–283.

903 McConnochie, C. D., and R. C. Kerr, 2016: The effect of a salinity gradient on the dissolution of
904 a vertical ice face. *Journal of Fluid Mechanics*, **791**, 589–607.

905 McConnochie, C. D., and R. C. Kerr, 2018: Dissolution of a sloping solid surface by turbulent
906 compositional convection. *J. Fluid Mech.*, **846**, 563–577.

907 McDougall, T. J., and P. M. Barker, 2011: Getting started with TEOS-10 and the Gibbs Seawater
908 (GSW) oceanographic toolbox. *SCOR/IAPSO WG*, **127**, 1–28.

909 McPhee, M. G., G. A. Maykut, and J. H. Morison, 1987: Dynamics and thermodynamics of the
910 ice/upper ocean system in the marginal ice zone of the Greenland Sea. *Journal of Geophysical*
911 *Research: Oceans*, **92 (C7)**, 7017–7031.

912 Middleton, L., C. A. Vreugdenhil, P. R. Holland, and J. R. Taylor, 2021: Numerical simulations of
913 melt-driven double-diffusive fluxes in a turbulent boundary layer beneath an ice shelf. *Journal*
914 *of Physical Oceanography*, **51 (2)**, 403–418.

915 Mkhinini, N., T. Dubos, and P. Drobinski, 2013: Secondary instability of the stably stratified
916 Ekman layer.

917 Moeng, C.-H., 1984: A large-eddy-simulation model for the study of planetary boundary-layer
918 turbulence. *Journal of the Atmospheric Sciences*, **41 (13)**, 2052–2062.

919 Mondal, M., B. Gayen, R. W. Griffiths, and R. C. Kerr, 2019: Ablation of sloping ice faces into
920 polar seawater. *Journal of Fluid Mechanics*, **863**, 545–571.

921 Nicholls, K., C. Pudsey, and P. Morris, 2004: Summertime water masses off the northern Larsen
922 C Ice Shelf, Antarctica. *Geophysical research letters*, **31 (9)**.

923 Nicholls, K. W., K. Makinson, and E. Venables, 2012: Ocean circulation beneath Larsen C Ice
924 Shelf, Antarctica from in situ observations. *Geophys. Res. Lett.*, **39**, L19 608.

925 Orszag, S. A., 1971: Numerical simulation of incompressible flows within simple boundaries. 1.
926 Galerkin (spectral) representation. *Stud. Appl. Maths*, **L**, 293.

- 927 Paolo, F. S., H. A. Fricker, and L. Padman, 2015: Volume loss from Antarctic ice shelves is
928 accelerating. *Science*, **348 (6232)**, 327–331.
- 929 Patmore, R. D., P. R. Holland, C. A. Vreugdenhil, A. Jenkins, and J. R. Taylor, in prep.: Turbulence
930 in the ice shelf–ocean boundary layer and its sensitivity to model resolution. *Journal of Physical*
931 *Oceanography*.
- 932 Piomelli, U., J. Ferziger, P. Moin, and J. Kim, 1989: New approximate boundary conditions for
933 large eddy simulations of wall-bounded flows. *Physics of Fluids A: Fluid Dynamics*, **1 (6)**,
934 1061–1068.
- 935 Pope, S. B., 2000: *Turbulent Flows*. Cambridge University Press, Cambridge, UK.
- 936 Pritchard, H., S. R. Ligtenberg, H. A. Fricker, D. G. Vaughan, M. R. van den Broeke, and L. Pad-
937 man, 2012: Antarctic ice-sheet loss driven by basal melting of ice shelves. *Nature*, **484 (7395)**,
938 502–505.
- 939 Rosevear, M. G., B. Gayen, and B. K. Galton-Fenzi, 2021: The role of double-diffusive convection
940 in basal melting of antarctic ice shelves. *Proceedings of the National Academy of Sciences*,
941 **118 (6)**.
- 942 Rozema, W., H. J. Bae, P. Moin, and R. Verstappen, 2015: Minimum-dissipation models for large-
943 eddy simulation. *Phys. Fluids*, **27**, 085 107.
- 944 Schlichting, H., and K. Gersten, 2003: *Boundary-Layer Theory*. Springer.
- 945 Schoof, C., 2007: Ice sheet grounding line dynamics: Steady states, stability, and hysteresis.
946 *Journal of Geophysical Research: Earth Surface*, **112 (F3)**.
- 947 Shepherd, A., D. Wingham, and E. Rignot, 2004: Warm ocean is eroding West Antarctic ice sheet.
948 *Geophysical Research Letters*, **31 (23)**.

- 949 Stanton, T. P., and Coauthors, 2013: Channelized ice melting in the ocean boundary layer beneath
950 Pine Island Glacier, Antarctica. *Science*, **341** (6151), 1236–1239.
- 951 Taylor, J. R., 2008: Numerical simulations of the stratified oceanic bottom boundary layer. Ph.D.
952 thesis, University of California, San Diego.
- 953 Verstappen, R., 2016: How much eddy dissipation is needed to counterbalance the nonlinear pro-
954 duction of small, unresolved scales in a large-eddy simulation of turbulence? *Comput. Fluids*,,
955 <http://dx.doi.org/10.1016/j.compfluid.2016.12.016>.
- 956 Vreugdenhil, C. A., and J. R. Taylor, 2018: Large-eddy simulations of stratified plane Couette
957 flow using the anisotropic minimum-dissipation model. *Physics of Fluids*, **30** (8), 085 104.
- 958 Vreugdenhil, C. A., and J. R. Taylor, 2019: Stratification effects in the turbulent boundary layer
959 beneath a melting ice shelf: Insights from resolved large-eddy simulations. *Journal of Physical*
960 *Oceanography*, **49** (7), 1905–1925.
- 961 Wyngaard, J. C., 2010: *Turbulence in the Atmosphere*. Cambridge University Press.
- 962 Zhou, Q., J. R. Taylor, and C. P. Caulfield, 2017: Self-similar mixing in stratified plane Couette
963 flow for varying Prandtl number. *J. Fluid Mech.*, **820**, 86–120.

964 **LIST OF TABLES**

965 **Table 1.** Constants used in the tidal forcing terms in the LES, based on Davis and
966 Nicholls (2019) observed values. The amplitudes have been multiplied by a
967 factor of 1.3 to result in maximum speeds that are on par with the observed val-
968 ues. Also note that we have converted Davis and Nicholls (2019)'s tidal ellipse
969 parameters into tidal amplitude and phase lag to use here. 46

970 TABLE 1. Constants used in the tidal forcing terms in the LES, based on Davis and Nicholls (2019) observed
 971 values. The amplitudes have been multiplied by a factor of 1.3 to result in maximum speeds that are on par with
 972 the observed values. Also note that we have converted Davis and Nicholls (2019)’s tidal ellipse parameters into
 973 tidal amplitude and phase lag to use here.

Mode	A_u (m/s)	A_v (m/s)	Φ_u (rad)	Φ_v (rad)	ω (rad/s)
O1	7.00×10^{-2}	4.68×10^{-2}	1.038	3.80	6.76×10^{-5}
K1	8.26×10^{-2}	4.46×10^{-2}	2.51	5.41	7.29×10^{-5}
M2	8.23×10^{-2}	1.51×10^{-2}	4.79	3.50	1.41×10^{-4}

974 **LIST OF FIGURES**

975 **Fig. 1.** Schematic showing the simulations of the ocean beneath the melting Larsen C Ice Shelf.
976 Left: map of Larsen C Ice Shelf with hot water drill access hole shown as green dot. The
977 colour contours show the ice base depth below sea level from Bedmap2 (Fretwell et al.
978 2013). Middle: simulated rectangular domain (not to scale) which is tilted in the x direction
979 to model the slope of the ice shelf base. The melt rate is a snapshot taken at Day 70 of the
980 large domain simulation. Right: tidal ellipses that match the three strongest modes from the
981 observations (Davis and Nicholls 2019). 50

982 **Fig. 2.** Time dependence of (a) far-field slope-parallel velocities and speed, (b) friction velocity
983 calculated at the ice base (u_* , Eqn. 7), (c) ice shelf melt rate, and (d) the mixed layer
984 depth for the large domain simulation. All results have been averaged in the slope-parallel
985 directions across the domain. On (c) the dotted line shows the year-averaged observed melt
986 rate (Davis and Nicholls 2019). The jumps in mixed layer depth are set by model resolution. 51

987 **Fig. 3.** Vertical profiles of (a) temperature and (b) salinity, vertical gradients of (c) temperature and
988 (d) salinity, and (e) the T - S diagram. The simulation profiles are shown at different points
989 in time and have been averaged in the slope-parallel directions across the domain. Note
990 that the topmost values of T , S are from the top of the water column (the first grid cell
991 beneath the ice) rather than being the ice-ocean boundary conditions T_b , S_b . Observations
992 from Larsen C Ice Shelf are also shown where CTD1 (dark green) was taken 7 hrs before
993 CTD2 (light green) (Nicholls et al. 2012; Davis and Nicholls 2019). The observed profiles
994 were smoothed using a moving average filter prior to the gradient being calculated for (c,
995 d), where the top and bottom 5% of the vertical gradient profiles are not shown as they are
996 outside the window of the moving average filter. In (e) the freezing point at the pressure of
997 the ice-base is shown as the dotted line. 52

998 **Fig. 4.** (a) Friction velocity and (b) drag coefficient against current speed, where u_*^{covar} was calcu-
999 lated using the covariance method (Eqn. 8). Line colour corresponds to the depth at which
1000 u_*^{covar} , C_d^{covar} , and current speed were calculated (blue = 2.5 m depth, red = 13.5 m depth).
1001 In the LES, all variables were averaged in the slope-parallel directions and the results are
1002 shown for Days 70 to 100 only. Also included are the Davis and Nicholls (2019) observa-
1003 tions over more than a year period for the Upper MAVS (2.5 m depth, light blue) and Lower
1004 MAVS (13.5 m depth, light pink) and the best fits to the observed data (black lines). (c) The
1005 evolution of the LES u_*^{covar} , along with u_* calculated at the ice base (Eqn. 7; orange line)
1006 and the far-field speed (dashed grey). The evolution of LES (d) u_*^{covar} , (e) speed, and (f)
1007 stratification in the uppermost 50 m of the domain for Day 76 (shaded region in (c)). 53

1008 **Fig. 5.** The (a) melt rate, (b) friction velocity and (c) drag coefficient against speed. The transfer
1009 coefficients for (d) heat and (e) salt, and (f) the drag coefficient with depth. The current speed
1010 and melt rate were averaged in the slope-parallel directions across the domain. The results
1011 are shown for Days 70 to 100 of the simulation only. In (a-c) the line colour corresponds
1012 to the depth at which C_d and the current speed were calculated (blue = 2.5m depth, red =
1013 13.5m depth and cyan = far-field at 190m depth). In (c, f) the drag coefficient was calculated
1014 using friction velocity at the ice base (Eqn. 7). 54

1015 **Fig. 6.** Snapshot taken at Day 70 for the large domain simulation shows the vertical velocity, tem-
1016 perature and slope-parallel speed of the three-dimensional flow. An isothermal (green line)
1017 of $T = -2.02^\circ\text{C}$ is shown on the vertical slice of temperature. The slope-parallel slice of
1018 speed is from 20 m depth, with the far-field speed and orientation also included for this time
1019 step (white arrow). The dashed rectangle on the slope-parallel slice demonstrates the size
1020 and orientation of the small domain simulation. 55

1021	Fig. 7.	Turbulent kinetic energy in wavenumber space (k, l). The TKE was calculated from a slope-parallel slice of velocity corresponding to the same time and depth shown in Figure 6 (Day 70, $z = -20$ m). Velocity fluctuations were taken with respect to values averaged in the slope-parallel directions. The green contour shows the chosen cut-off TKE = 3×10^{-9} m^2s^{-2}	56
1022			
1023			
1024			
1025			
1026	Fig. 8.	The evolution of the Ekman rolls at depth $z = -20$ m. (a) Mean current speed of the flow at $z = -20$ m, (b) roll width, (c) roll angle, and (d) averaged turbulent kinetic energy TKE. The TKE has been averaged across the slope-parallel slice at $z = -20$ m for each time step. The total of this average TKE is shown, along with the portion associated with the Ekman rolls. The Ekman roll portion of TKE was calculated using the chosen cut-off in wavenumber space (cut off value of TKE = 3×10^{-9} m^2s^{-2} for the large domain grid resolution).	57
1027			
1028			
1029			
1030			
1031			
1032	Fig. 9.	Snapshot taken at Day 70 for the small domain simulation shows the vertical velocity, temperature and slope-parallel speed of the three-dimensional flow. An isothermal (green line) of $T = -2.02^\circ\text{C}$ is shown on the vertical slice of temperature. The slope-parallel slice of speed is from 10 m depth, with the far-field speed and orientation also included for this time step (white arrow).	58
1033			
1034			
1035			
1036			
1037	Fig. 10.	The resolved versus sub-grid scale contributions for the vertical heat flux at different depths. (a) The sub-grid scale heat diffusivity κ_{SGS} for the large (low resolution) and small (high resolution) domain simulations. The vertical heat flux of the resolved and sub-grid scale contributions for (b) the large domain and (c) the small domain. All values have been averaged in the slope-parallel directions across the domain, and averaged in time for the duration of the reinitialised simulations (Day 52 to Day 78). Note that results are shown for the top 100 m only, and that the zero line is plotted in (b) and (c) as a thin black dotted line.	59
1038			
1039			
1040			
1041			
1042			
1043			
1044	Fig. 11.	Partitioning of the turbulent kinetic energy and vertical heat flux into the contribution from the Ekman rolls for the small domain (high resolution) simulation. The slope-parallel averaged speed of the far-field current is included in (a) for reference. The averaged (in the x' direction) TKE partitioning is shown for (b) $z = -10$ m and (d) $z = -20$ m. The averaged (in the x' direction) vertical heat flux partitioning is shown for (c) $z = -10$ m and (e) $z = -20$ m. A cumulative sum of the vertical heat flux is shown for both depths in (f). Each figure (b)–(f) shows the total (cyan) and the component just associated with the Ekman rolls (blue). Also shown in (c), (e), and (f) is the resolved contribution to the vertical heat transport (pink). The cumulative sum in (f) has been normalised so that the final vertical heat flux value equals the time-mean across the total interval, for ease of comparison with Figure 10. The partitioning was done using the TKE cutoff of 6×10^{-6} m^2s^{-2} , which is equivalent to the TKE cutoff used in Figures 7 and 8 for the large domain simulation.	60
1045			
1046			
1047			
1048			
1049			
1050			
1051			
1052			
1053			
1054			
1055			
1056	Fig. 12.	Vertical profiles of (a) temperature and (b) salinity for the small domain (high resolution) simulation. The simulation profiles are shown at different points in time and have been averaged in the slope-parallel directions across the domain. Note that the topmost values of T, S are from the top of the water column (the first grid cell beneath the ice) rather than being the ice-ocean boundary conditions T_b, S_b	61
1057			
1058			
1059			
1060			
1061	Fig. 13.	Time evolution and wavelet analysis for a point measurement at depth $z = -20$ m in the large domain simulation, where the time sampling was approximately 16 seconds for the interval shown. The point measurement time series of (a) the two slope-parallel velocity components, (b) the temperature, and (c) the resulting wavelet transform for just the temperature measurement. The white dashed line is the M2 tidal component, the other two tidal components K1, O1 are at periods slightly larger than the interval shown. The wavelet transform	
1062			
1063			
1064			
1065			
1066			

1067 uses Generalized Morse Wavelets with $\gamma = 3$ and $\beta = 2$ (please refer to the jLab MATLAB
 1068 toolbox by Lilly (2017) for the meaning and detailed discussion of these parameters). 62

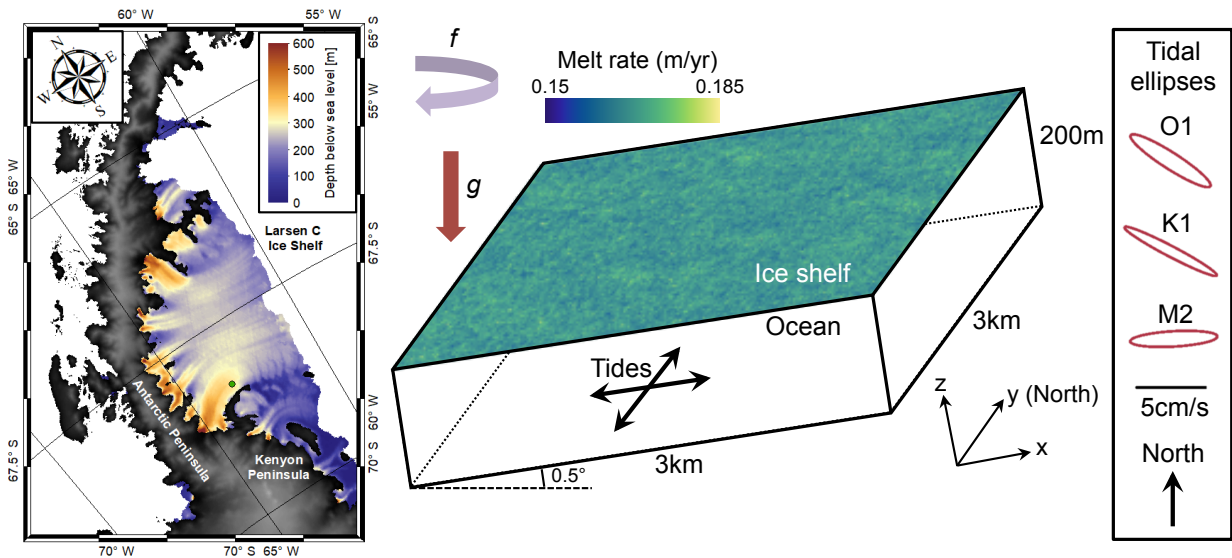
1069 **Fig. B1.** Near-wall model (NWM) validation: transfer coefficients of (a) heat Γ_T and (b) salt Γ_S ,
 1070 and (c) drag coefficient C_d (Eqn. B14) against Obukhov length scale ratio L^+ , and (d) melt
 1071 rate against thermal driving $\Delta T = T_{z=-2m} - T_b$. The results from resolved LES of the upper
 1072 2m below the ice base reported in Vreugdenhil and Taylor (2019) are shown as the solid
 1073 symbols (and thick lines), and results using the derived near-wall model with the first grid
 1074 point within the log layer (8cm from base of the ice) are shown as the open symbols (and
 1075 thin lines). Colours show two different friction velocities. Solid lines are $u_* = 0.05$ cm/s
 1076 cases and dashed lines are $u_* = 0.1$ cm/s cases. In (a)-(c), the red lines show the Monin-
 1077 Obukhov scaling that the near-wall model is based on. The lines in panel (d) correspond to
 1078 the passive scalar limit. 63

1079 **Fig. B2.** The Obukhov length scale ratio L^+ with time for the large domain near-wall model LES. 64

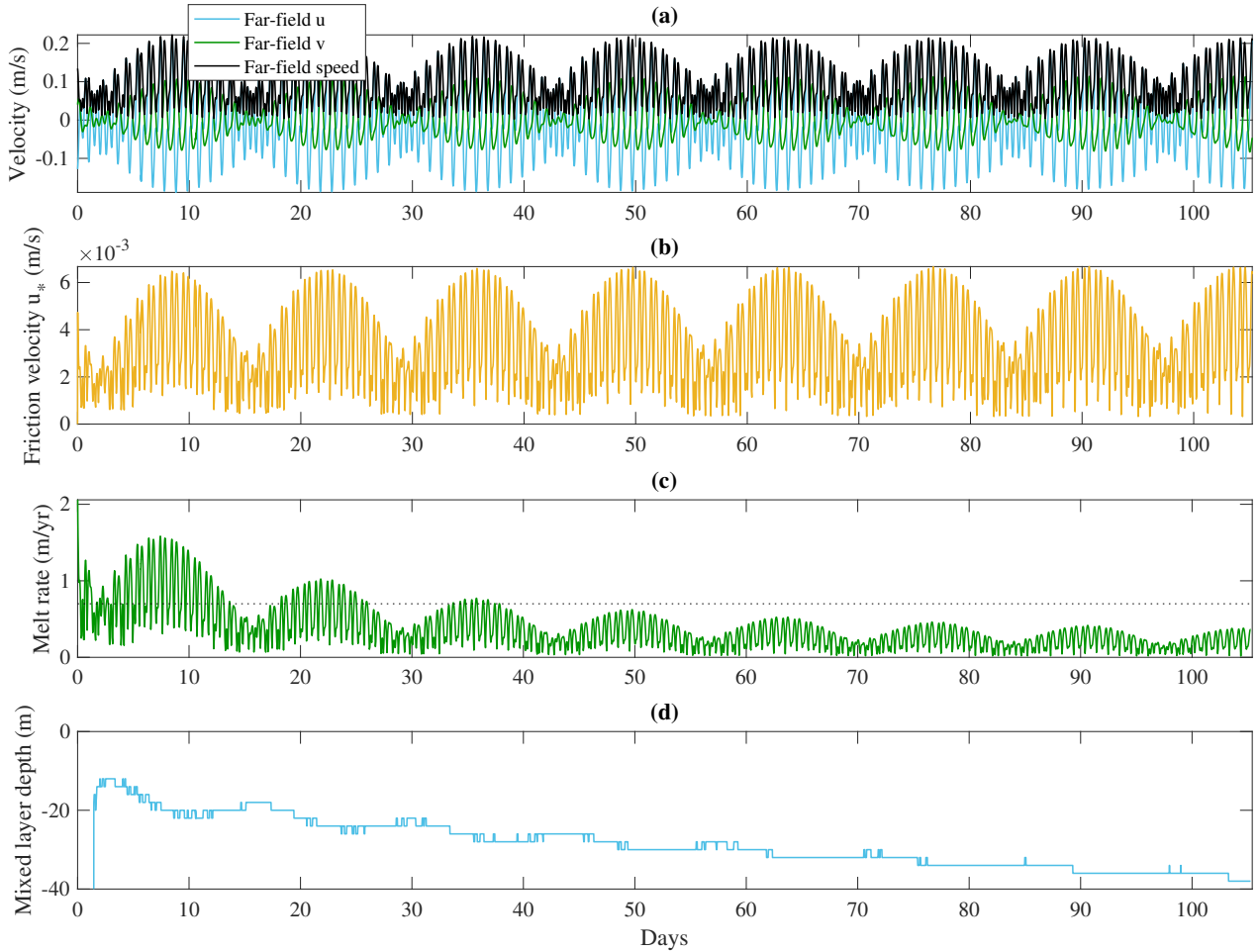
1080 **Fig. C1.** Vertical profiles of slope-parallel velocity (a, c) u and (b, d) v for the simulations with ice
 1081 base slope (a, b) and no slope (c, d). The simulation profiles are shown at different points in
 1082 time and have been averaged in the slope-parallel directions across the domain. The dotted
 1083 lines show the Ekman layer depth, $\sqrt{2\nu_{SGS}/f}$, where $\nu_{SGS} \approx 10^{-3} \text{ m}^2\text{s}^{-1}$ was the maximum
 1084 turbulent viscosity. Note that the topmost values of u, v are from the first grid cell beneath
 1085 the ice rather than being the ice-ocean boundary conditions which are no-slip (zero u, v). 65

1086 **Fig. C2.** The (a) melt rate, (b) friction velocity and (c) drag coefficient against speed for a simulation
 1087 with no slope. The transfer coefficients for (d) heat and (e) salt, and (f) the drag coefficient
 1088 with depth for a simulation with no slope. The current speed and melt rate were averaged
 1089 in the slope-parallel directions across the domain. The results are shown for Days 70 to 100
 1090 of the simulation only. In (a-c) the line colour corresponds to the depth at which C_d and the
 1091 current speed were calculated (blue = 2.5m depth, red = 13.5m depth and cyan = far-field at
 1092 190m depth). In (c, f) the drag coefficient was calculated using friction velocity at the ice
 1093 base (Eqn. 7). 66

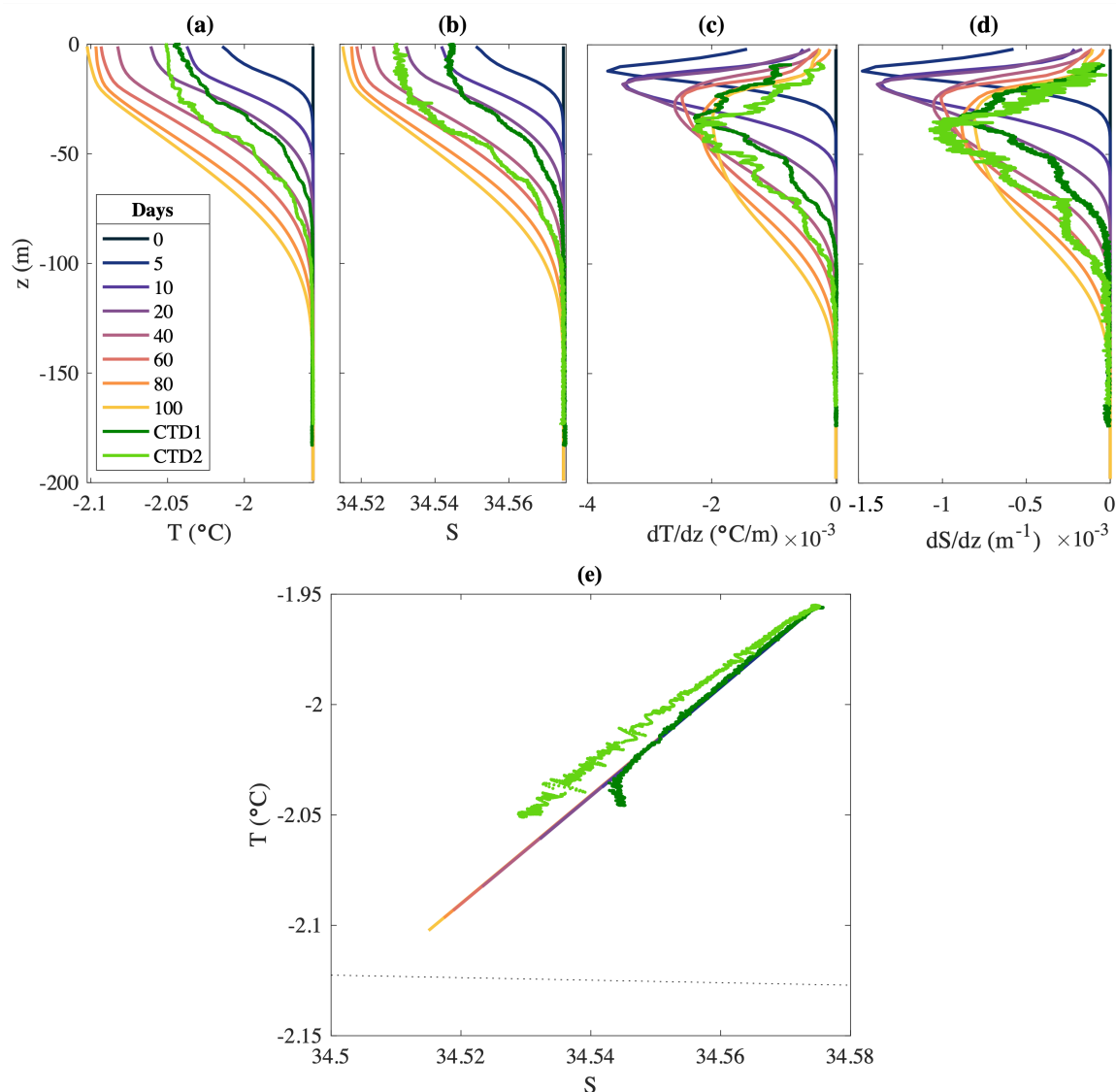
1094 **Fig. C3.** The evolution of the Ekman rolls at depth $z = -20$ m for a simulation with no slope. (a)
 1095 Mean current speed of the flow at $z = -20$ m, (b) roll width, (c) roll angle, and (d) averaged
 1096 turbulent kinetic energy TKE. The TKE has been averaged across the slope-parallel slice
 1097 at $z = -20$ m for each time step. The total of this average TKE is shown, along with the
 1098 portion associated with the Ekman rolls. The Ekman roll portion of TKE was calculated
 1099 using the chosen cut-off in wavenumber space (cut off value of $\text{TKE} = 3 \times 10^{-9} \text{ m}^2\text{s}^{-2}$ for
 1100 the large domain grid resolution). 67



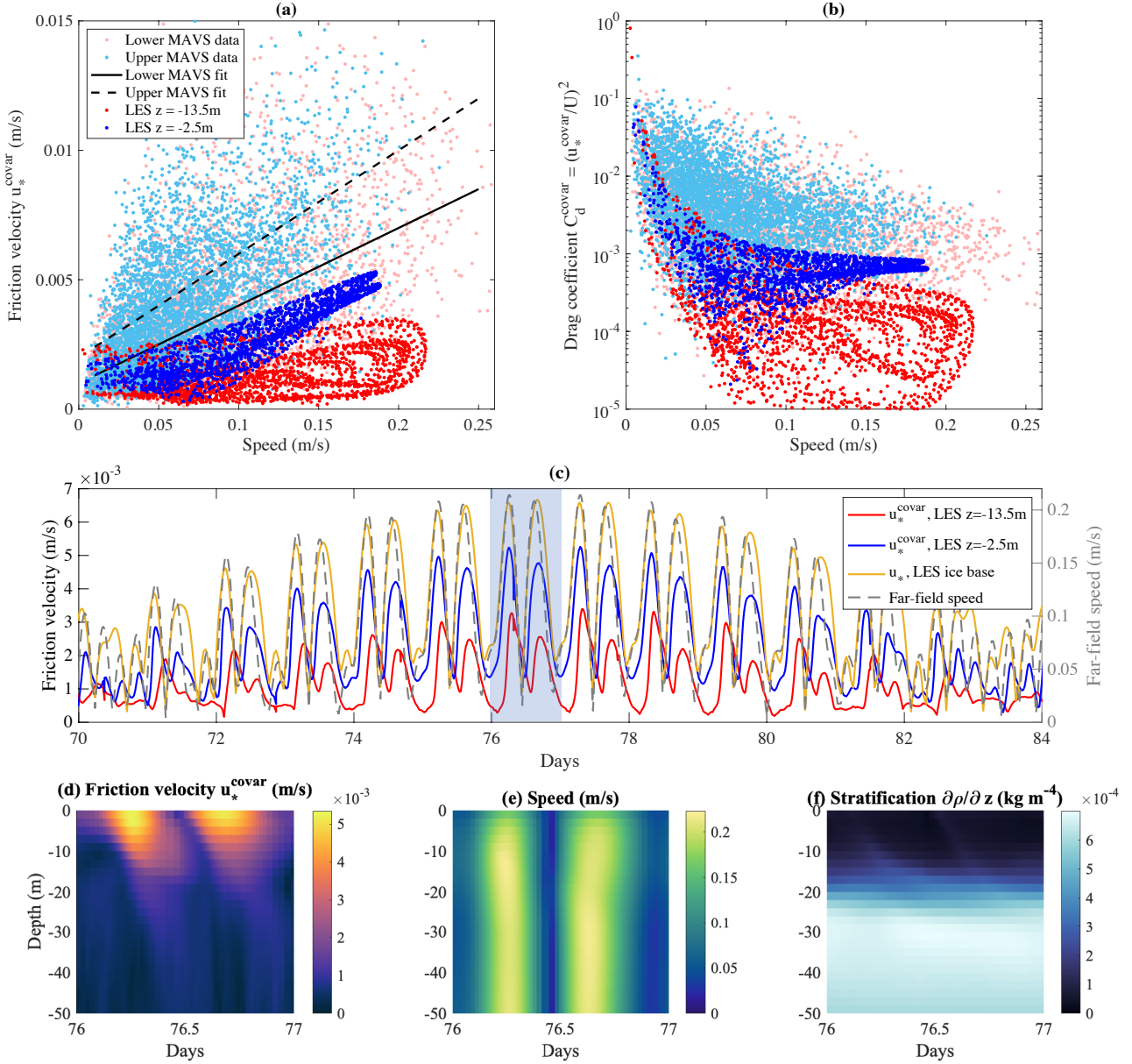
1101 FIG. 1. Schematic showing the simulations of the ocean beneath the melting Larsen C Ice Shelf. Left: map
 1102 of Larsen C Ice Shelf with hot water drill access hole shown as green dot. The colour contours show the ice
 1103 base depth below sea level from Bedmap2 (Fretwell et al. 2013). Middle: simulated rectangular domain (not to
 1104 scale) which is tilted in the x direction to model the slope of the ice shelf base. The melt rate is a snapshot taken
 1105 at Day 70 of the large domain simulation. Right: tidal ellipses that match the three strongest modes from the
 1106 observations (Davis and Nicholls 2019).



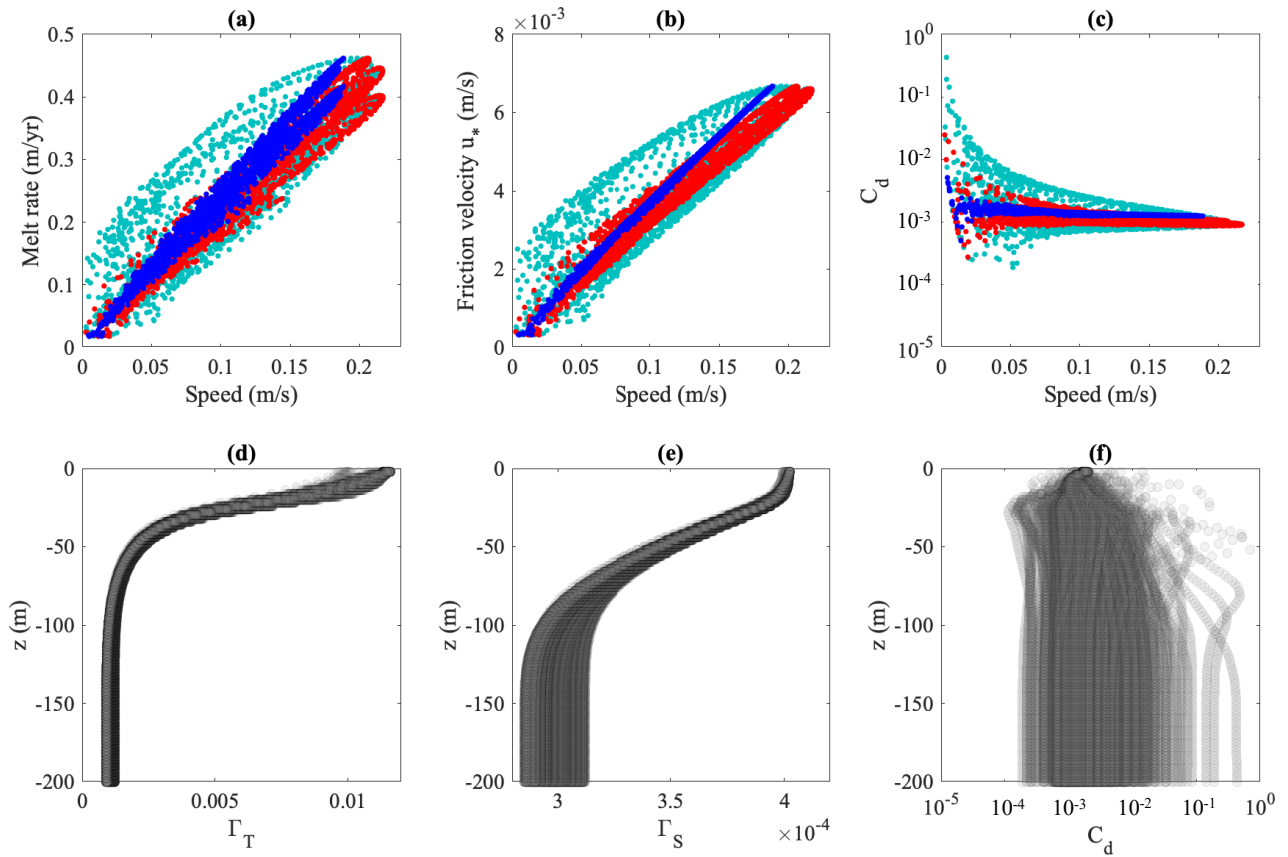
1107 FIG. 2. Time dependence of (a) far-field slope-parallel velocities and speed, (b) friction velocity calculated at
 1108 the ice base (u_* , Eqn. 7), (c) ice shelf melt rate, and (d) the mixed layer depth for the large domain simulation.
 1109 All results have been averaged in the slope-parallel directions across the domain. On (c) the dotted line shows
 1110 the year-averaged observed melt rate (Davis and Nicholls 2019). The jumps in mixed layer depth are set by
 1111 model resolution.



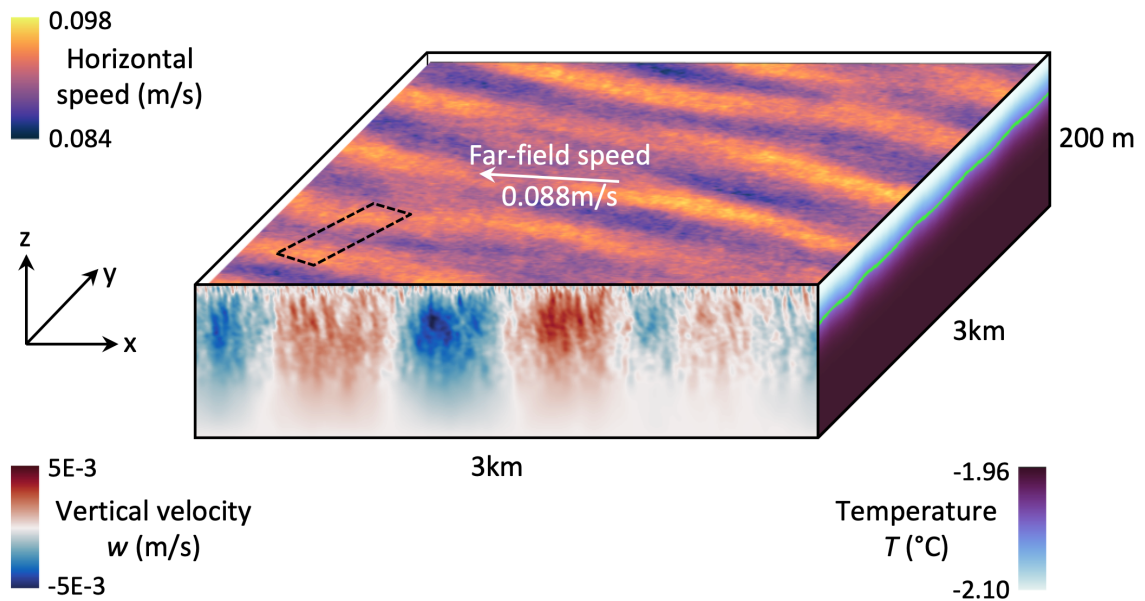
1112 FIG. 3. Vertical profiles of (a) temperature and (b) salinity, vertical gradients of (c) temperature and (d)
 1113 salinity, and (e) the T - S diagram. The simulation profiles are shown at different points in time and have been
 1114 averaged in the slope-parallel directions across the domain. Note that the topmost values of T , S are from the
 1115 top of the water column (the first grid cell beneath the ice) rather than being the ice-ocean boundary conditions
 1116 T_b , S_b . Observations from Larsen C Ice Shelf are also shown where CTD1 (dark green) was taken 7 hrs before
 1117 CTD2 (light green) (Nicholls et al. 2012; Davis and Nicholls 2019). The observed profiles were smoothed using
 1118 a moving average filter prior to the gradient being calculated for (c, d), where the top and bottom 5% of the
 1119 vertical gradient profiles are not shown as they are outside the window of the moving average filter. In (e) the
 1120 freezing point at the pressure of the ice-base is shown as the dotted line.



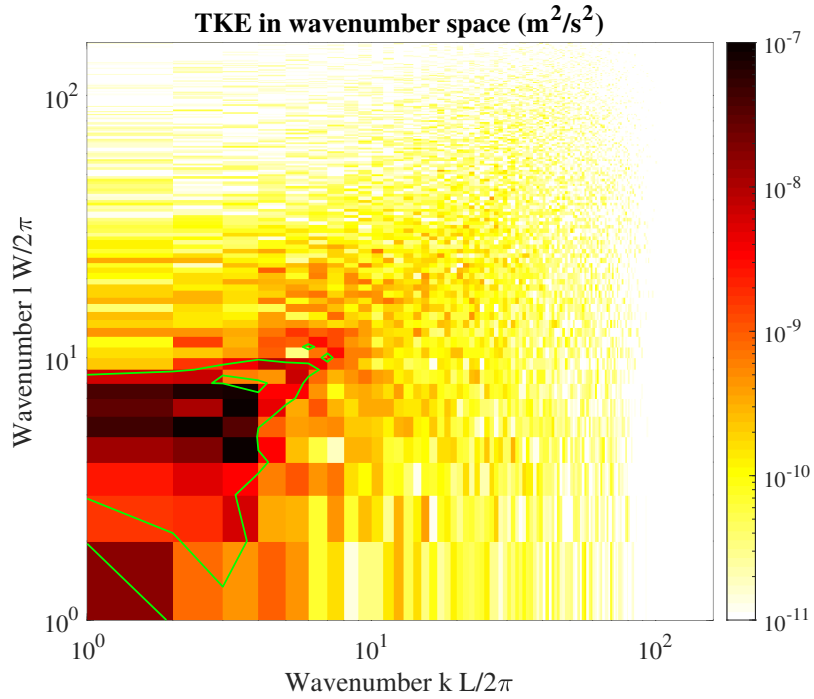
1121 FIG. 4. (a) Friction velocity and (b) drag coefficient against current speed, where u_*^{covar} was calculated using
 1122 the covariance method (Eqn. 8). Line colour corresponds to the depth at which u_*^{covar} , C_d^{covar} , and current speed
 1123 were calculated (blue = 2.5 m depth, red = 13.5 m depth). In the LES, all variables were averaged in the slope-
 1124 parallel directions and the results are shown for Days 70 to 100 only. Also included are the Davis and Nicholls
 1125 (2019) observations over more than a year period for the Upper MAVS (2.5 m depth, light blue) and Lower
 1126 MAVS (13.5 m depth, light pink) and the best fits to the observed data (black lines). (c) The evolution of the
 1127 LES u_*^{covar} , along with u_* calculated at the ice base (Eqn. 7; orange line) and the far-field speed (dashed grey).
 1128 The evolution of LES (d) u_*^{covar} , (e) speed, and (f) stratification in the uppermost 50 m of the domain for Day 76
 1129 (shaded region in (c)).



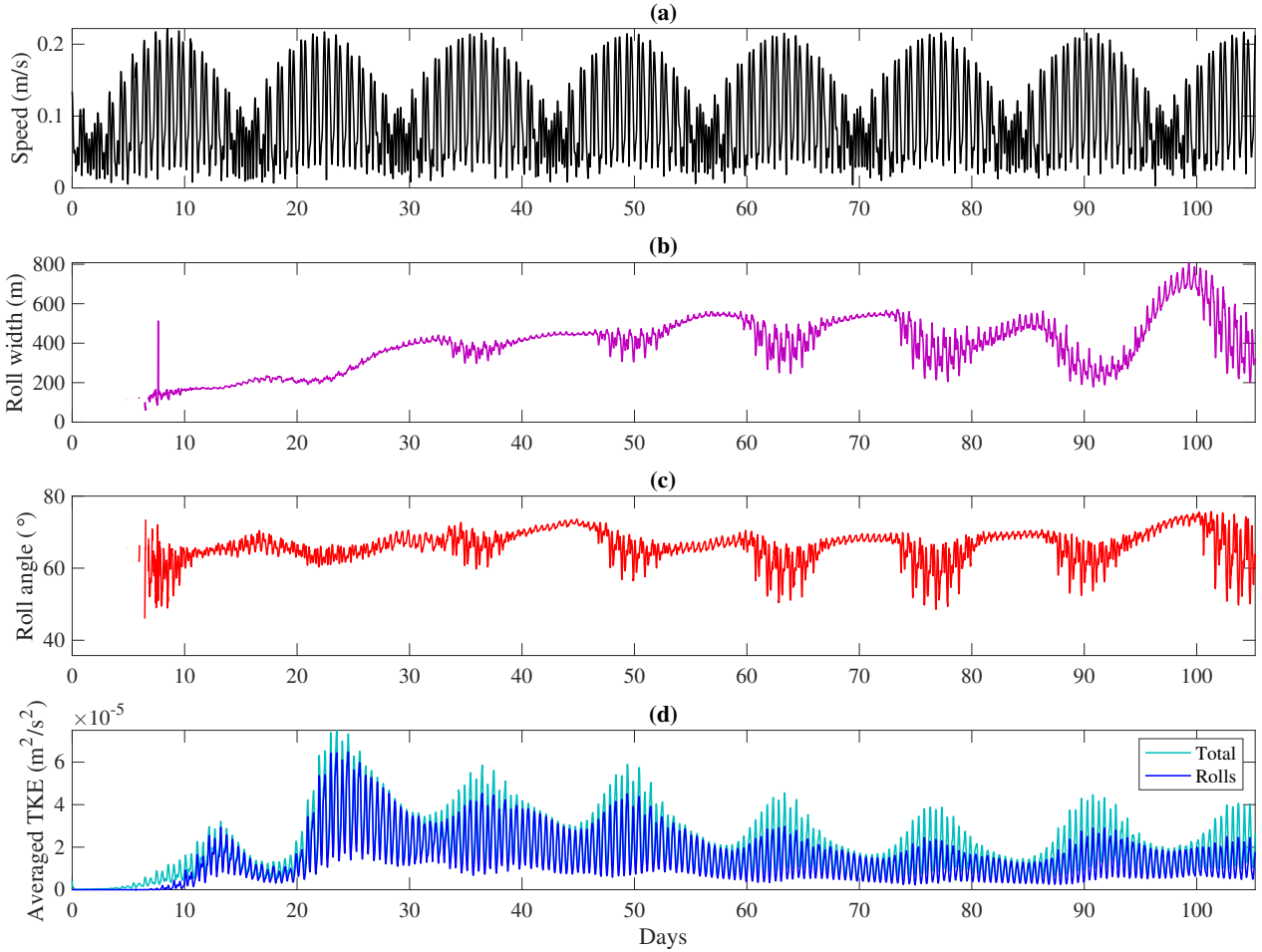
1130 FIG. 5. The (a) melt rate, (b) friction velocity and (c) drag coefficient against speed. The transfer coefficients
 1131 for (d) heat and (e) salt, and (f) the drag coefficient with depth. The current speed and melt rate were averaged
 1132 in the slope-parallel directions across the domain. The results are shown for Days 70 to 100 of the simulation
 1133 only. In (a-c) the line colour corresponds to the depth at which C_d and the current speed were calculated (blue =
 1134 2.5m depth, red = 13.5m depth and cyan = far-field at 190m depth). In (c, f) the drag coefficient was calculated
 1135 using friction velocity at the ice base (Eqn. 7).



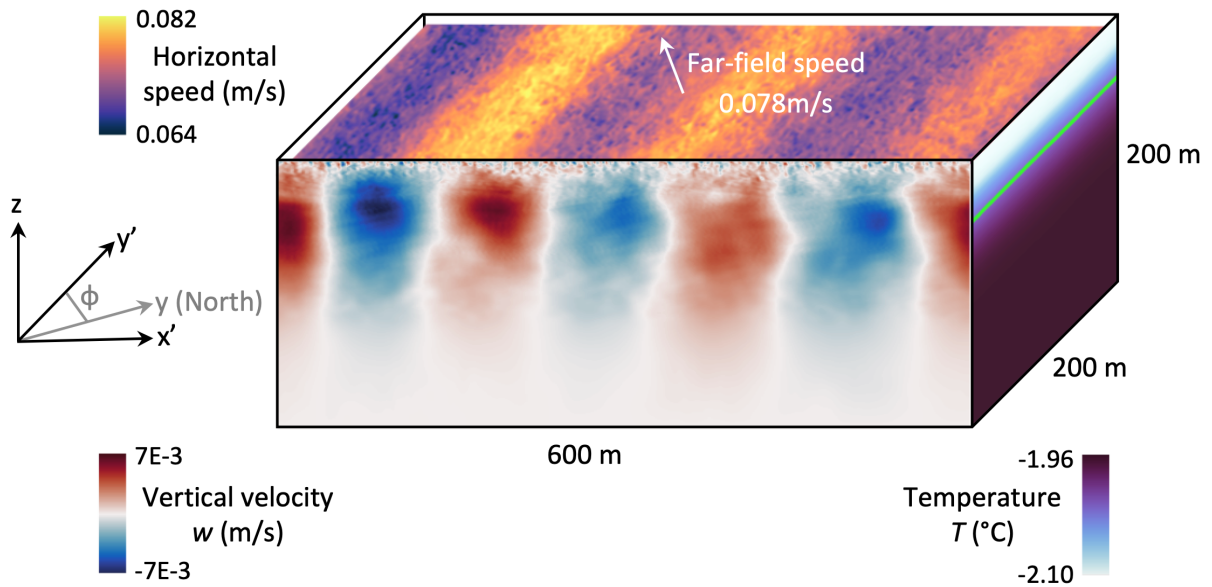
1136 FIG. 6. Snapshot taken at Day 70 for the large domain simulation shows the vertical velocity, temperature
 1137 and slope-parallel speed of the three-dimensional flow. An isothermal (green line) of $T = -2.02^{\circ}\text{C}$ is shown on
 1138 the vertical slice of temperature. The slope-parallel slice of speed is from 20 m depth, with the far-field speed
 1139 and orientation also included for this time step (white arrow). The dashed rectangle on the slope-parallel slice
 1140 demonstrates the size and orientation of the small domain simulation.



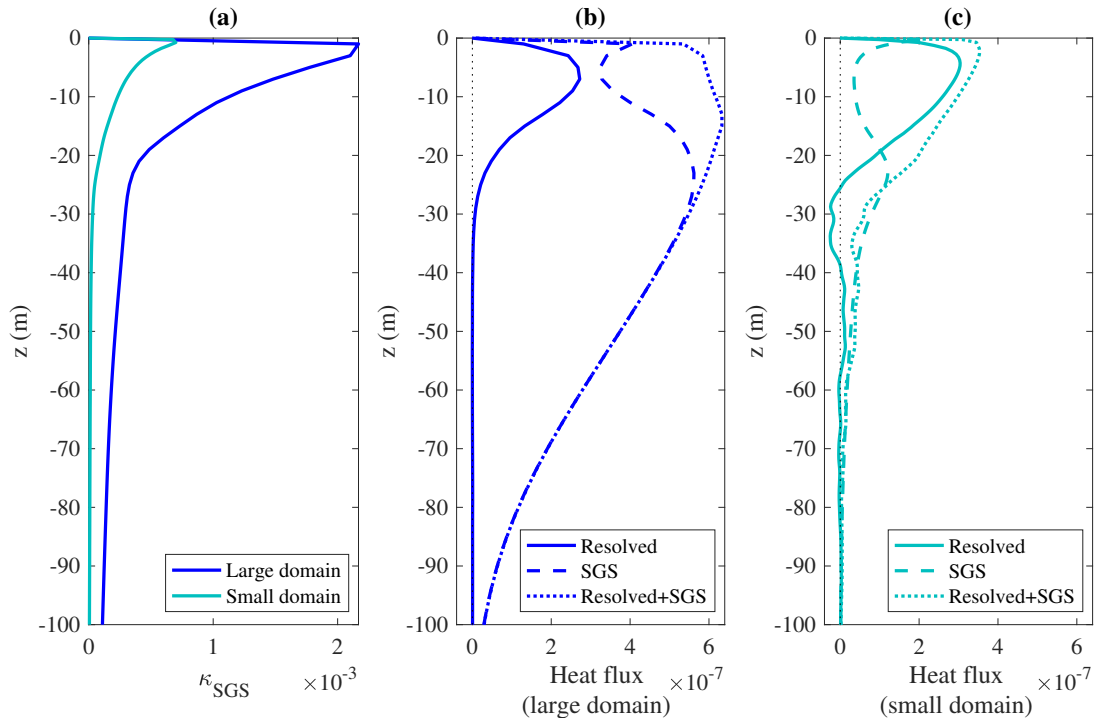
1141 FIG. 7. Turbulent kinetic energy in wavenumber space (k, l). The TKE was calculated from a slope-parallel
 1142 slice of velocity corresponding to the same time and depth shown in Figure 6 (Day 70, $z = -20$ m). Velocity
 1143 fluctuations were taken with respect to values averaged in the slope-parallel directions. The green contour shows
 1144 the chosen cut-off TKE = $3 \times 10^{-9} \text{ m}^2\text{s}^{-2}$.



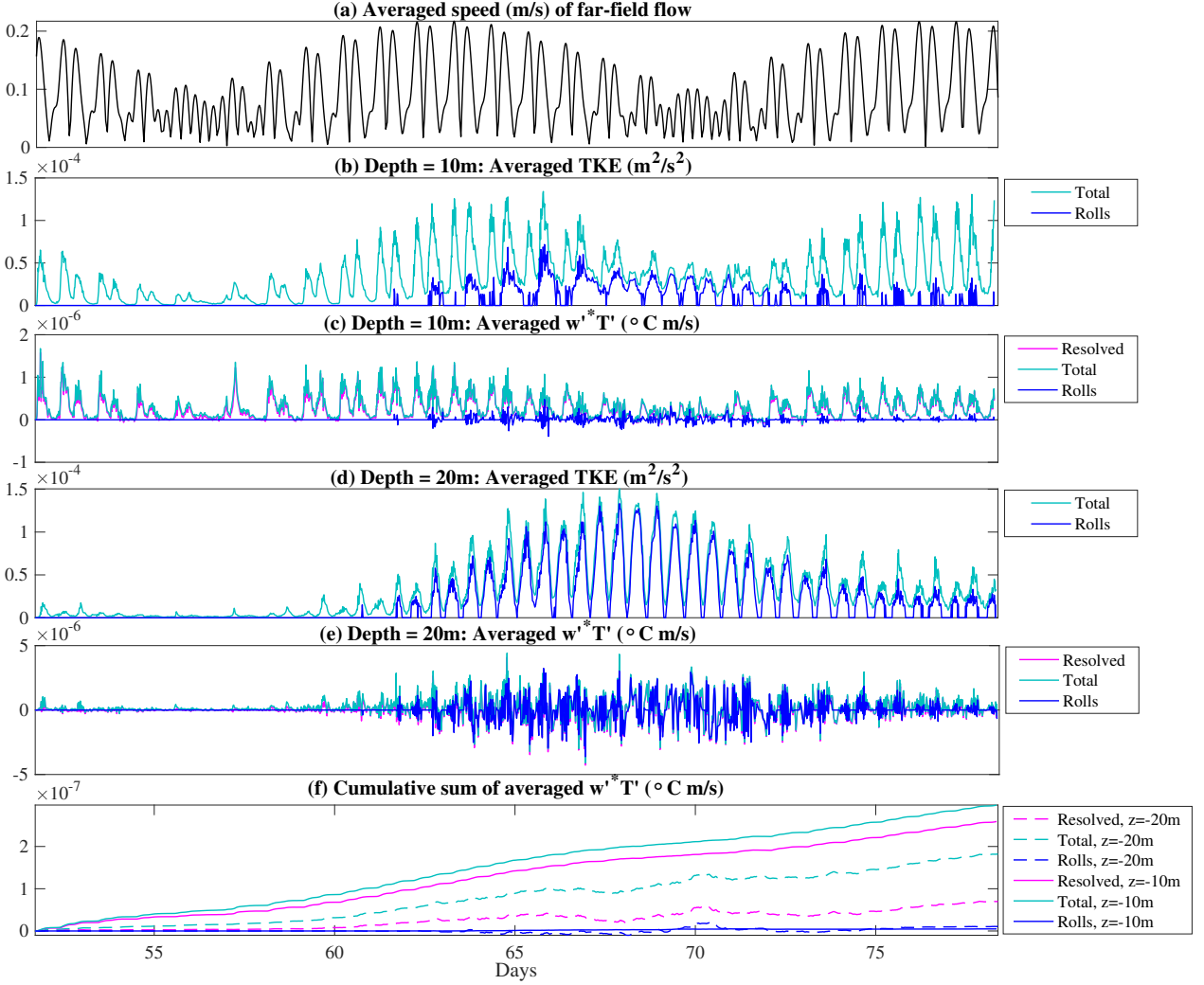
1145 FIG. 8. The evolution of the Ekman rolls at depth $z = -20$ m. (a) Mean current speed of the flow at $z = -20$ m,
 1146 (b) roll width, (c) roll angle, and (d) averaged turbulent kinetic energy TKE. The TKE has been averaged across
 1147 the slope-parallel slice at $z = -20$ m for each time step. The total of this average TKE is shown, along with the
 1148 portion associated with the Ekman rolls. The Ekman roll portion of TKE was calculated using the chosen cut-off
 1149 in wavenumber space (cut off value of $\text{TKE} = 3 \times 10^{-9} \text{ m}^2 \text{ s}^{-2}$ for the large domain grid resolution).



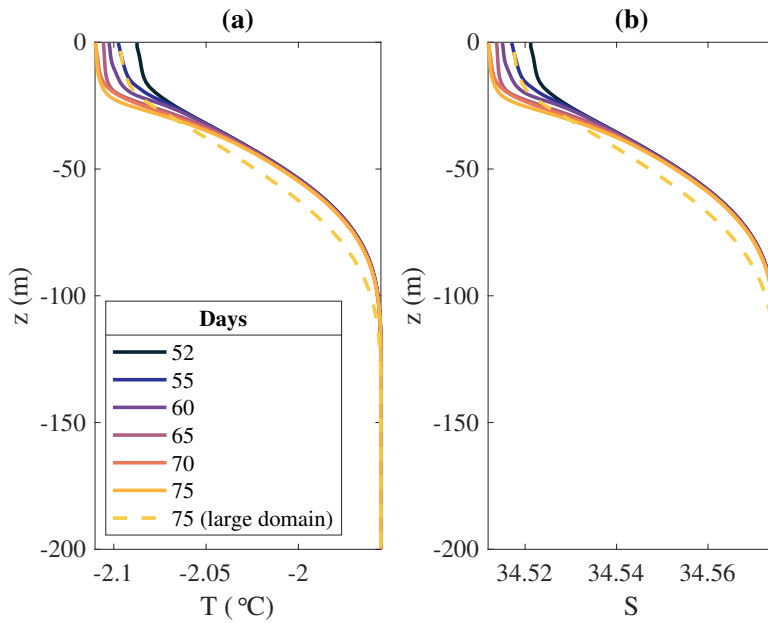
1150 FIG. 9. Snapshot taken at Day 70 for the small domain simulation shows the vertical velocity, temperature
 1151 and slope-parallel speed of the three-dimensional flow. An isothermal (green line) of $T = -2.02^\circ\text{C}$ is shown on
 1152 the vertical slice of temperature. The slope-parallel slice of speed is from 10 m depth, with the far-field speed
 1153 and orientation also included for this time step (white arrow).



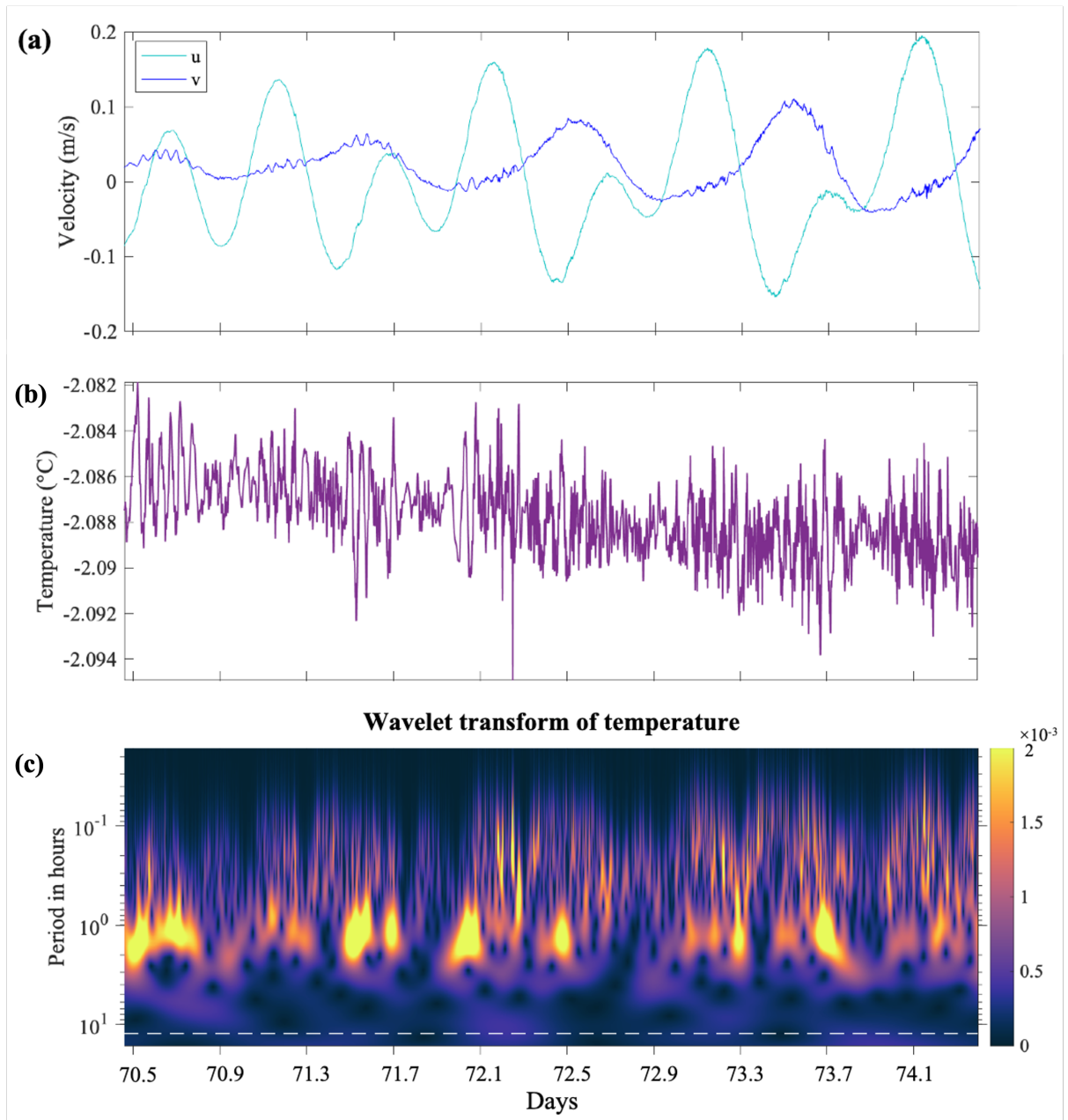
1154 FIG. 10. The resolved versus sub-grid scale contributions for the vertical heat flux at different depths. (a) The
 1155 sub-grid scale heat diffusivity κ_{SGS} for the large (low resolution) and small (high resolution) domain simulations.
 1156 The vertical heat flux of the resolved and sub-grid scale contributions for (b) the large domain and (c) the small
 1157 domain. All values have been averaged in the slope-parallel directions across the domain, and averaged in time
 1158 for the duration of the reinitialised simulations (Day 52 to Day 78). Note that results are shown for the top 100
 1159 m only, and that the zero line is plotted in (b) and (c) as a thin black dotted line.



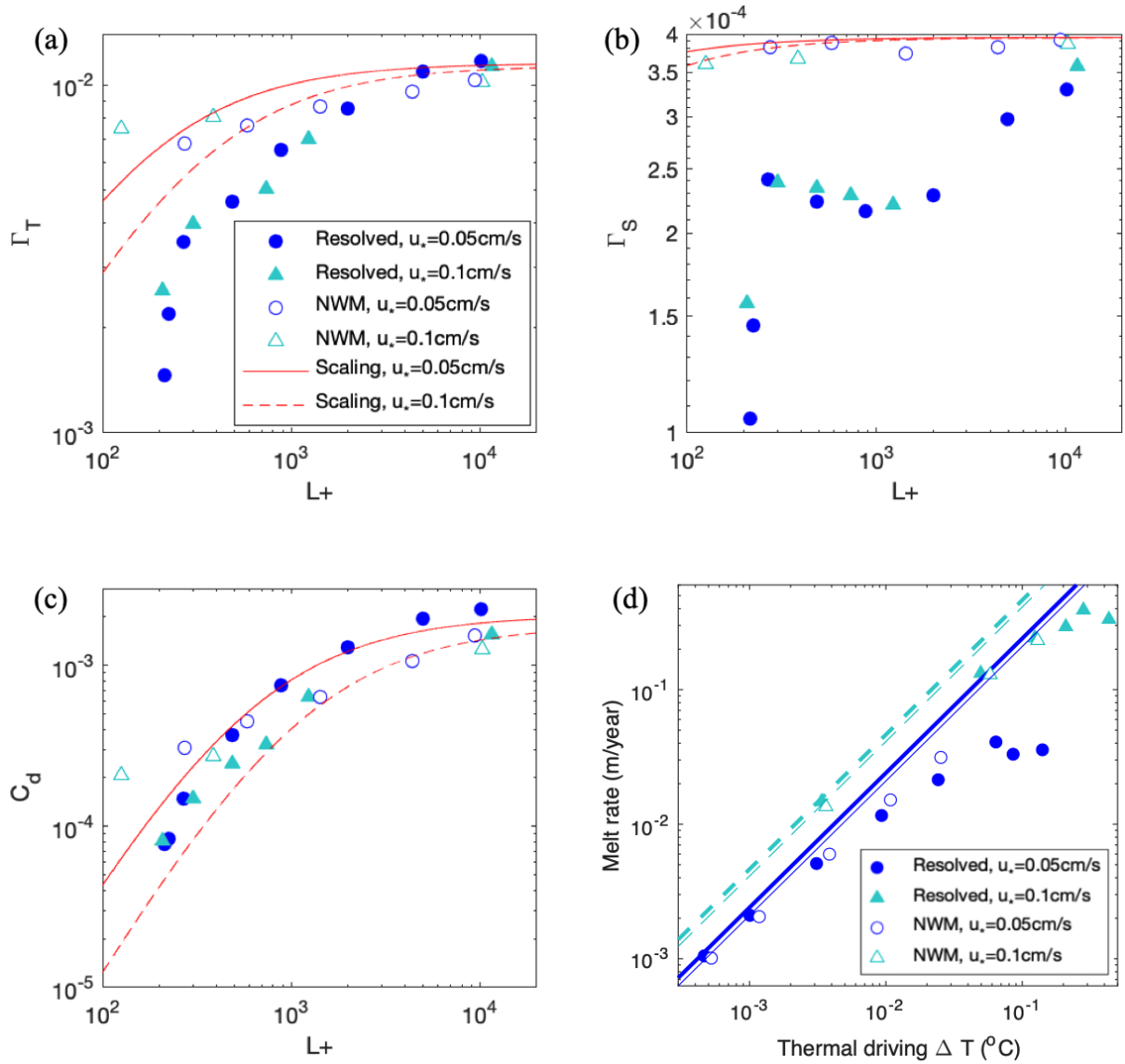
1160 FIG. 11. Partitioning of the turbulent kinetic energy and vertical heat flux into the contribution from the
 1161 Ekman rolls for the small domain (high resolution) simulation. The slope-parallel averaged speed of the far-field
 1162 current is included in (a) for reference. The averaged (in the x' direction) TKE partitioning is shown for (b)
 1163 $z = -10$ m and (d) $z = -20$ m. The averaged (in the x' direction) vertical heat flux partitioning is shown for (c)
 1164 $z = -10$ m and (e) $z = -20$ m. A cumulative sum of the vertical heat flux is shown for both depths in (f). Each
 1165 figure (b)–(f) shows the total (cyan) and the component just associated with the Ekman rolls (blue). Also shown
 1166 in (c), (e), and (f) is the resolved contribution to the vertical heat transport (pink). The cumulative sum in (f)
 1167 has been normalised so that the final vertical heat flux value equals the time-mean across the total interval, for
 1168 ease of comparison with Figure 10. The partitioning was done using the TKE cutoff of $6 \times 10^{-6} \text{ m}^2\text{s}^{-2}$, which
 1169 is equivalent to the TKE cutoff used in Figures 7 and 8 for the large domain simulation.



1170 FIG. 12. Vertical profiles of (a) temperature and (b) salinity for the small domain (high resolution) simulation.
 1171 The simulation profiles are shown at different points in time and have been averaged in the slope-parallel direc-
 1172 tions across the domain. Note that the topmost values of T , S are from the top of the water column (the first grid
 1173 cell beneath the ice) rather than being the ice-ocean boundary conditions T_b , S_b .



1174 FIG. 13. Time evolution and wavelet analysis for a point measurement at depth $z = -20$ m in the large domain
 1175 simulation, where the time sampling was approximately 16 seconds for the interval shown. The point measure-
 1176 ment time series of (a) the two slope-parallel velocity components, (b) the temperature, and (c) the resulting
 1177 wavelet transform for just the temperature measurement. The white dashed line is the M2 tidal component, the
 1178 other two tidal components K1, O1 are at periods slightly larger than the interval shown. The wavelet transform
 1179 uses Generalized Morse Wavelets with $\gamma = 3$ and $\beta = 2$ (please refer to the jLab MATLAB toolbox by Lilly
 1180 (2017) for the meaning and detailed discussion of these parameters).



1181 Fig. B1. Near-wall model (NWM) validation: transfer coefficients of (a) heat Γ_T and (b) salt Γ_S , and (c)
 1182 drag coefficient C_d (Eqn. B14) against Obukhov length scale ratio L^+ , and (d) melt rate against thermal driving
 1183 $\Delta T = T_{z=-2m} - T_b$. The results from resolved LES of the upper 2m below the ice base reported in Vreugdenhil
 1184 and Taylor (2019) are shown as the solid symbols (and thick lines), and results using the derived near-wall model
 1185 with the first grid point within the log layer (8cm from base of the ice) are shown as the open symbols (and thin
 1186 lines). Colours show two different friction velocities. Solid lines are $u_* = 0.05$ cm/s cases and dashed lines are
 1187 $u_* = 0.1$ cm/s cases. In (a)-(c), the red lines show the Monin–Obukhov scaling that the near-wall model is based
 1188 on. The lines in panel (d) correspond to the passive scalar limit.

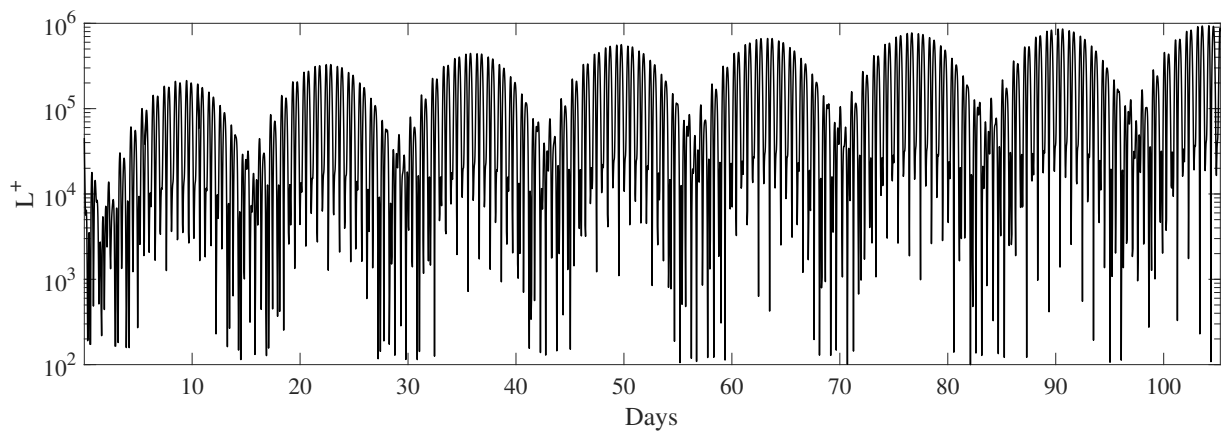
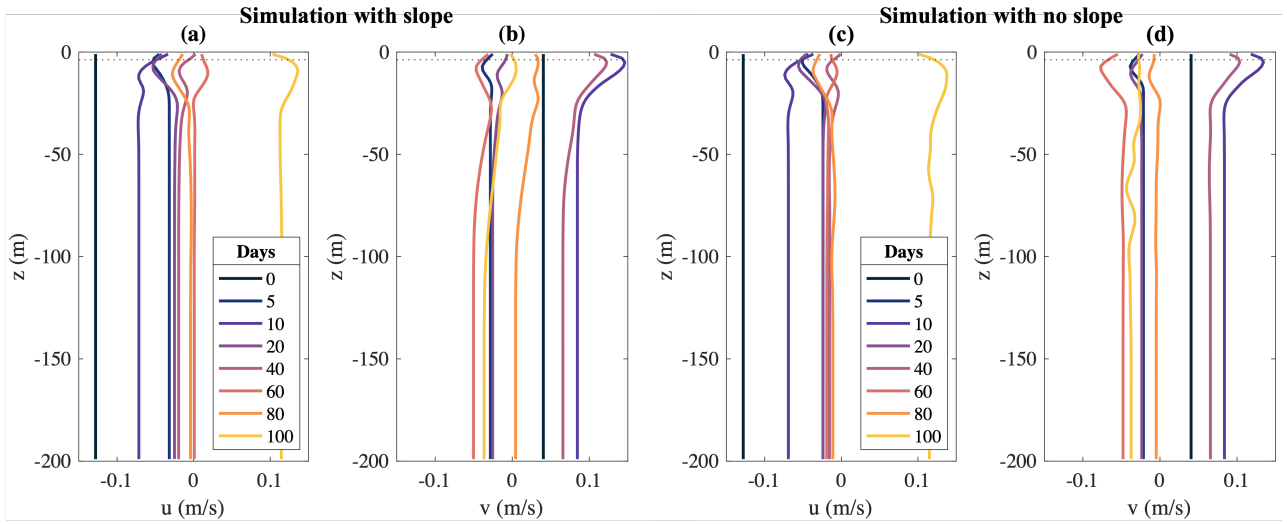
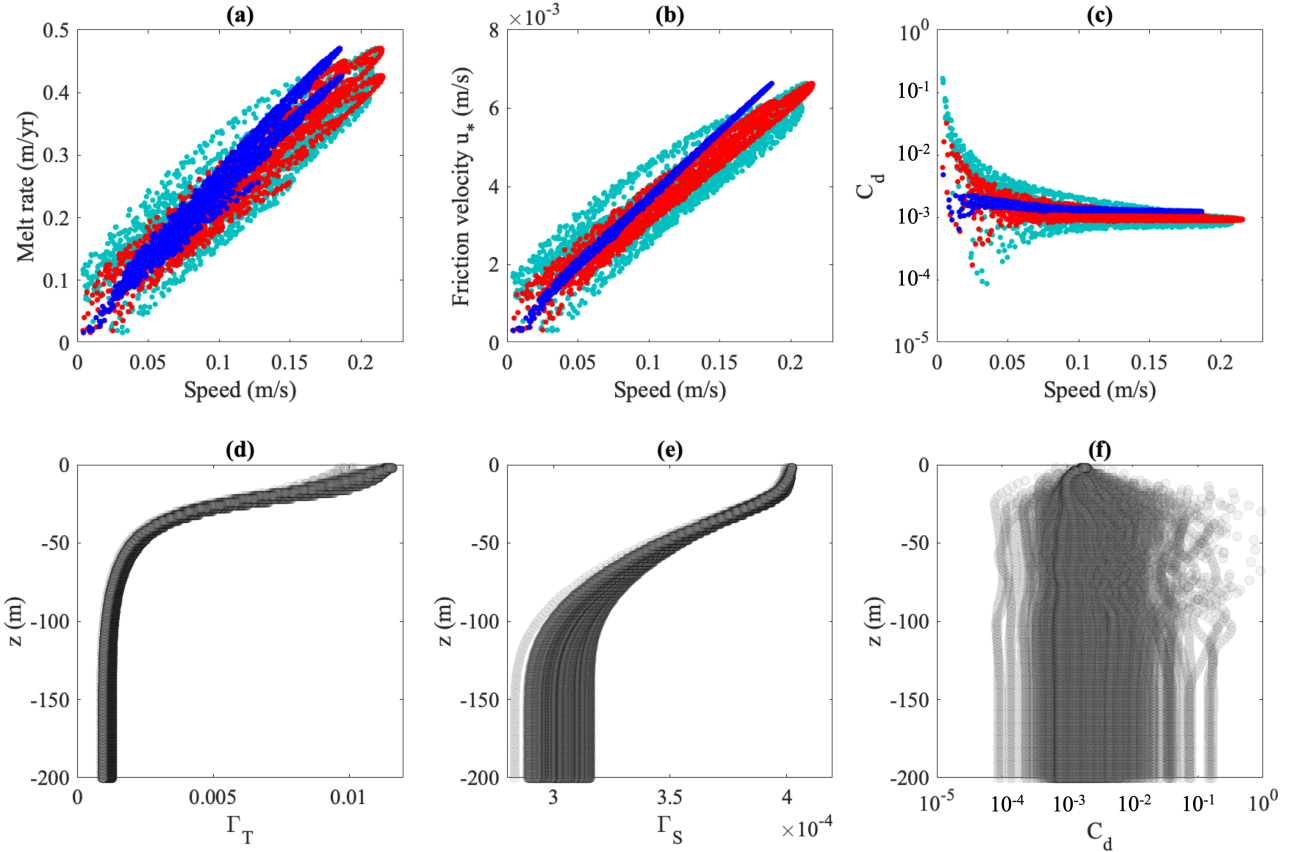


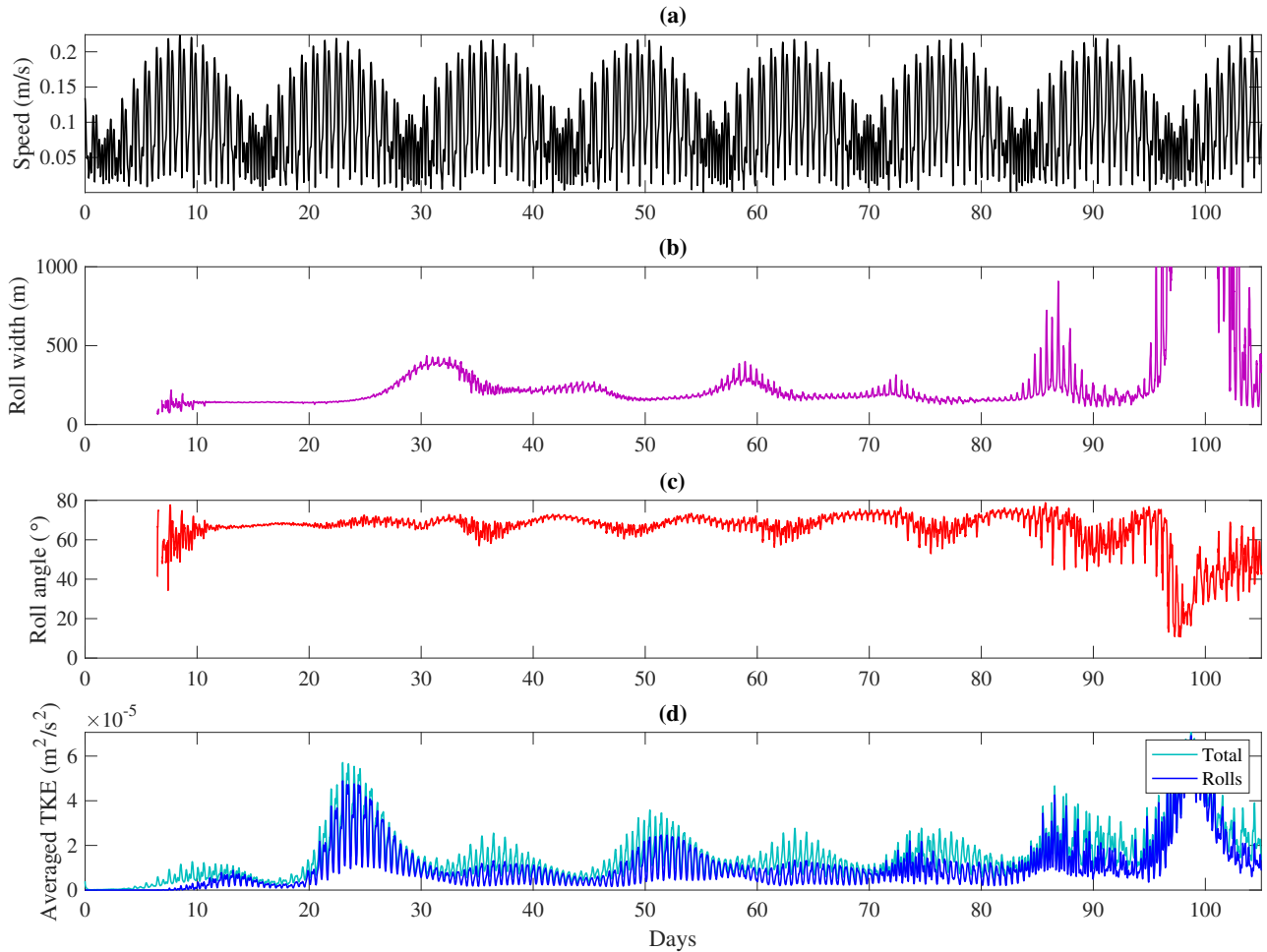
Fig. B2. The Obukhov length scale ratio L^+ with time for the large domain near-wall model LES.



1189 Fig. C1. Vertical profiles of slope-parallel velocity (a, c) u and (b, d) v for the simulations with ice base slope
 1190 (a, b) and no slope (c, d). The simulation profiles are shown at different points in time and have been averaged
 1191 in the slope-parallel directions across the domain. The dotted lines show the Ekman layer depth, $\sqrt{2\nu_{SGS}/f}$,
 1192 where $\nu_{SGS} \approx 10^{-3} \text{ m}^2\text{s}^{-1}$ was the maximum turbulent viscosity. Note that the topmost values of u , v are from
 1193 the first grid cell beneath the ice rather than being the ice-ocean boundary conditions which are no-slip (zero u ,
 1194 v).



1195 Fig. C2. The (a) melt rate, (b) friction velocity and (c) drag coefficient against speed for a simulation with no
 1196 slope. The transfer coefficients for (d) heat and (e) salt, and (f) the drag coefficient with depth for a simulation
 1197 with no slope. The current speed and melt rate were averaged in the slope-parallel directions across the domain.
 1198 The results are shown for Days 70 to 100 of the simulation only. In (a-c) the line colour corresponds to the depth
 1199 at which C_d and the current speed were calculated (blue = 2.5m depth, red = 13.5m depth and cyan = far-field at
 1200 190m depth). In (c, f) the drag coefficient was calculated using friction velocity at the ice base (Eqn. 7).



1201 Fig. C3. The evolution of the Ekman rolls at depth $z = -20$ m for a simulation with no slope. (a) Mean
 1202 current speed of the flow at $z = -20$ m, (b) roll width, (c) roll angle, and (d) averaged turbulent kinetic energy
 1203 TKE. The TKE has been averaged across the slope-parallel slice at $z = -20$ m for each time step. The total of
 1204 this average TKE is shown, along with the portion associated with the Ekman rolls. The Ekman roll portion of
 1205 TKE was calculated using the chosen cut-off in wavenumber space (cut off value of $\text{TKE} = 3 \times 10^{-9} \text{ m}^2\text{s}^{-2}$ for
 1206 the large domain grid resolution).